

Numerical Model of Early Continent Formation

Emma Havens

Department of Earth and Planetary Sciences, Northwestern University

Contents

1	Introduction	1
2	Background	2
3	Methods	3
3.1	Mathematical Design	3
3.1.1	Stokes Equation	3
3.1.2	Thermal Equation	4
3.1.3	Viscosity	4
3.1.4	Nondimensionalization	4
3.2	Numerical Methods	5
3.2.1	Spatial Discretization	6
3.2.2	Advection	6
3.2.3	Interpolation	9
3.2.4	Gaussian Quadrature	12
3.3	MATLAB Model Design	14
3.3.1	Initialization and Loop Steps	14
3.3.2	Model Parameters	15
3.3.3	Spatial Discretization and Model Geometry	15
3.3.4	Temporal Discretization	15
3.3.5	Markers	16
3.3.6	Nodes	16
3.3.7	Thermal Solver	17
3.3.8	Mechanical Solver	18
3.3.9	Reseeding Routine	18
3.3.10	Save Variables	18
3.4	Quantification and Measurement of Results	18
3.4.1	Rate of Crustal Building	18
3.4.2	Rate of Mantle Mixing	19
3.4.3	Crustal Reworking	19
4	Results	19
4.0.1	Base Cases	19
4.0.2	Effect of Aspect Ratio	22
4.0.3	Effect of Water Fugacity	26
4.0.4	Result Table	28

1 Introduction

Continents are essential to the development of life on Earth. Dissolved and eroded continental rock flows to the oceans in runoff and reacts with ocean water, causing net removal of CO₂ from the atmosphere. The ability to both remove CO₂ and re-release it via volcanic gasses allows Earth to have long term climate stability that makes it habitable (Hawkesworth and Kemp, 2006). Understanding how the continents were able to form will give insight into what led to habitability on this planet and not on others (Hastie et al., 2023; Lammer et al., 2009). It can also clarify the relationship between tectonic events, climate stability, and biological innovation, which may have been

a major driver for evolution (Lowe and Tice, 2006). However, the formation process of Earth's first continents is not fully understood, and crucial factors such as water content, silica content, and temperature of the early Earth's interior are poorly constrained (Boehnke et al., 2018; Dong et al., 2021; Korenaga, 2011).

Plate tectonics are an expression of mantle convection at the surface. Modern continental crust is created by reworking and remelting existing crust at subduction zones, which emplaces melt into or on existing continental crust (Hastie et al., 2023). High silica content in the crust increases the density contrast between the crust and the mantle, which helps the crust resist subduction and increases its survivability (Korenaga, 2021). Water can decrease viscosity, thus increasing the convective velocity and the stresses that are exerted on the continents and increasing subduction rates (Korenaga, 2011). However, it also lowers the melting point of the rock, which increases production of lower temperature and higher buoyancy silica-rich melts (Thompson, 1992). High mantle temperatures may lead to less viscous mantle rock, but it also becomes drier and lowers its water content, making temperature's effect on viscosity unclear (Korenaga, 2011).

Density and viscosity are included in the equations typically used to model mantle rock flow and continental crust generation and recycling, as described in 3.1. Understanding how water content, silica content, and mantle temperature relate to density and viscosity allows us to create numerical models that can explore how the onset of continental crust formation, the rate of continental crust generation, and the persistence of continental crust at the surface is altered due to varying temperatures and compositions.

2 Background

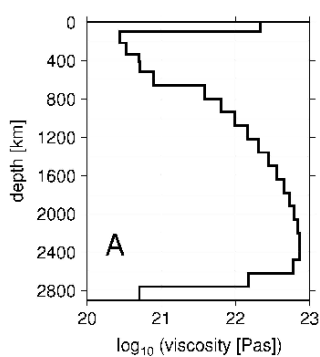


Figure 1: Viscosity profile for Earth. Depth is along the y axis. Modified from Steinberger and Becker (2012)

The mechanical properties of minerals are governed by the creation and motion of imperfections, or defects, in the atomic lattice structure. The migration of vacancies, which are holes in the lattice where there is typically an atom, is one manner in which rock can flow; this regime is called diffusion creep. Rock can also flow through dislocation creep, which involves the migration of linear defects called dislocations, which are a local rearrangement of atoms within a lattice rather than a singular absent atom. Viscosity is the measure of a fluid's resistance to flow, so for mantle rock, viscosity is governed by factors that affect defects.

The viscosity of the crust and mantle is largely controlled by temperature, pressure and mineral structure; temperature increases the mobility of vacancies and pressure decreases the mobility. Viscosity can be averaged according to depth in order to achieve a radial viscosity profile for Earth, depicted in Fig 1. For the average profile, this results in a highly viscous, stiff lithosphere, a less viscous upper mantle, a highly viscous lower mantle, and a less viscous core mantle boundary. The large perturbations in viscosity at the top and bottom of the mantle are due to the effect of temperature. The effect of temperature on viscosity can also cause deviations from this average profile in sites of downwelling or upwelling.

Viscosity can also be influenced by the water content of the rock. Olivine can have point defects in the form of vacancies. Water can enter these vacancies as an O-H, which causes a decrease in viscosity (Mei and Kohlstedt, 2000). Water fugacity is a measurement quantifying the amount of water in a rock, and is used to describe the impact of water on viscosity in Section 3.1.3. Figure 2 displays the relationship between strain rate (which is inversely related to viscosity, see Section 3.1.3) and water fugacity.

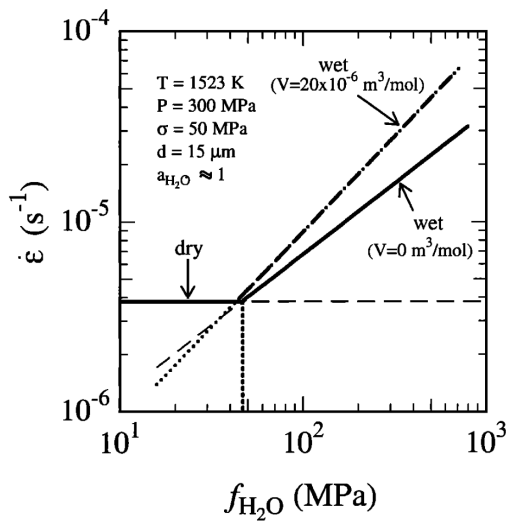


Figure 2: A log-log plot of strain rate versus water fugacity. Dry and wet markers refer to whether the tested sample was hydrous or anhydrous rock. (Mei and Kohlstedt, 2000)

3 Methods

3.1 Mathematical Design

The mantle undergoes thermochemical convection, which is described by equations of conservation of mass, momentum, and energy. The nondimensional conservation equations that are utilized in the numerical model are described below.

3.1.1 Stokes Equation

The Stokes equation (1) describes the conservation of momentum for mantle convection. The Stokes equation's first term describes how pressure varies in space, the second term describes the buoyancy force, and the third describes the rate of deformation caused by the divergence of deviatoric stress.

$$0 = \frac{\partial p}{\partial x_i} + Ra(T + BrC)g_i - \frac{\partial \tau_{ij}}{\partial x_j} \quad (1)$$

$$Ra = \frac{\rho g \alpha \Delta T D^3}{\mu \kappa} \quad (2)$$

$$Br = \frac{\rho_C - \rho_M}{\alpha \rho \Delta T} \quad (3)$$

$$\tau_{ij} = 2\mu \epsilon_{ij} = \mu \left(\frac{\partial v_i}{\partial x_j} + \frac{\partial v_j}{\partial x_i} \right) \quad (4)$$

In the above equations, the subscript i refers to the direction (either x or y), x_i is the component of the position vector in the direction of i , p pressure, T temperature of the mantle, C chemical composition, g_i the component of the gravity acceleration vector in the direction of i , τ_{ij} the ij components of the deviatoric stress tensor, ρ density, α thermal conductivity, ΔT temperature difference between the top and bottom of the mantle, D depth of the mantle, μ viscosity, κ thermal diffusivity, ρ_C continent compositional density, ρ_M mantle compositional density, ϵ_{ij} the ij components of the strain rate, and v_i the component of the velocity vector in the direction of i .

The buoyancy force term utilizes Equations 2 and 3, which are the Raleigh number (Ra) and the buoyancy ratio (Br), respectively. The Raleigh number describes the vigor of convection, with a higher Ra meaning a more vigorous convection, and a lower Ra being a more sluggish one. The buoyancy ratio describes the chemical composition induced density variation compared to thermal induced density variation. A negative Br means the overlying layer is less compositionally dense than the underlying layer and is positively buoyant, while a positive Br means the overlying layer is more compositionally dense than the underlying layer and is negatively buoyant. A Br of 0 means there are no chemically induced density differences, and any convection is purely thermal convection. A high Ra and Br would lead to an increase in the buoyancy force term of equation 1, which would mandate an increase in deviatoric stress, higher rates of deformation, and higher velocities.

The deviatoric stress term utilizes Equation 4, which is describing the rate of deformation caused by deviatoric stress. Equation 4 is written assuming that the rate of deformation (strain rate) and the deviatoric stresses in the Earth's mantle is linearly dependant (a Newtonian fluid). It also assumes that it is isotropic (the constants describing the relation are independent of orientation in space) and incompressible (the volume of a given parcel doesn't change according to pressure).

3.1.2 Thermal Equation

The thermal equation 5 examines how the temperature of a point evolves through time as it is advected through space, as described by the material derivative $\frac{D}{Dt}$. The material derivative $\frac{D}{Dt}$ is defined in Equation 6.

$$\frac{DT}{Dt} = \frac{\partial}{\partial x_i} \left(\frac{\partial T}{\partial x_i} \right) \quad (5)$$

$$\frac{DT}{Dt} = \frac{\partial T}{\partial t} + \frac{\partial T}{\partial x} \frac{\partial x}{\partial t} + \frac{\partial T}{\partial y} \frac{\partial y}{\partial t} + \frac{\partial T}{\partial z} \frac{\partial z}{\partial t} \quad (6)$$

T is temperature, t time, x_i position vector, x , y , and z are components of the position vector.

Equation 5 is greatly simplified due to assuming there is no internal heat generation. That is, Equation 5 assumes there is no heat generated due to radiogenic decay or deformational work. All heat is transferred through movement of material and thermal conduction.

Equation 6 well illustrates how a solution for $\frac{D}{Dt}$ involves the solution for two separate processes. The temperature of the mantle evolves through both diffusion, where heat attempts to disperse unrelated to the movement of the material, and advection, where heat is transported through the movement of the material. The first term, $\frac{\partial T}{\partial t}$, describes thermal diffusion; the last three terms describe thermal advection.

3.1.3 Viscosity

Viscosity μ can be described in terms of strain rate ε_{ij} and deviatoric stress τ_{ij} . Equation 7 is a rearrangement of Equation 4 and describes the relationship between μ , ε_{ij} , and τ_{ij} within a diffusion creep regime, which is dominant in the mantle.

$$\mu = \frac{\tau_{ij}}{2\varepsilon_{ij}} \quad (7)$$

Approximations for ε_{ij} , such as those made by Mei and Kohlstedt (2000), can thus be rearranged to approximate μ . Within a diffusion creep regime, μ is not dependent on ε_{ij} and τ_{ij} .

$$\mu = \mu_0 \cdot f_{H_2O} \cdot \exp\left(\frac{H}{XRT}\right) \quad (8)$$

$$H = Q + PV \quad (9)$$

with μ_0 a reference viscosity, T temperature, f_{H_2O} water fugacity, H activation enthalpy, R gas law constant, X scaling constant, Q activation energy, P pressure, and V activation volume.

In Equation 8, μ is dependent on temperature, water fugacity, and activation enthalpy, which defines a minimum amount of enthalpy needed for temperature to influence viscosity. In the model, these will be the mechanisms that can influence viscosity.

3.1.4 Nondimensionalization

Unless otherwise specified below, all variables have been nondimensionalized in the following way:

$$x = x' \bar{x} \quad (10)$$

Where x is a variable found in above equations, \bar{x} is a quantity from Table 1, and x' is an amount departure from the dimensional value.

Quantity	Symbol	Dimensional Values	Dimensions
Gravitational Acceleration	\bar{g}	10	m s^{-2}
Thermal Expansivity	$\bar{\alpha}$	$1 \cdot 10^{-5}$	K^{-1}
Density	$\bar{\rho}$	$3.2 \cdot 10^3$	kg m^{-3}
Temperature Drop Across Mantle	$\bar{\Delta T}$	3215	K
Mantle Depth	\bar{D}	$2.9 \cdot 10^6$	m
Thermal Diffusivity	$\bar{\kappa}$	$6 \cdot 10^{-7}$	$\text{m}^2 \text{s}^{-1}$
Dynamic Viscosity	$\bar{\mu}$	$5 \cdot 10^{21}$	Pa s
Activation Enthalpy	\bar{H}	350	kJ mol^{-1}
Water Fugacity	\bar{f}_{H_2O}	$1 \cdot 10^{-1}$	MPa
Raleigh Number	\bar{Ra}	$1 \cdot 10^7$	1

Table 1: Values used to describe geophysical properties of the mantle. Prime indicates dimensional quality of parameter.

Many values from table 1 are from (Mulyukova, 2015). $\bar{\rho}$ has been altered to be more representative of the upper mantle, rather than the lower mantle.

Density has been nondimensionalized in the following way:

$$\rho' = \frac{\rho - \bar{\rho}}{\bar{\alpha} \bar{\rho} \bar{\Delta T}} \quad (11)$$

Where ρ' , ρ , and $\bar{\rho}$ are nondimensionalized, dimensionalized, and reference densities, $\bar{\alpha}$ is thermal expansivity, and $\bar{\Delta T}$ is temperature drop across the mantle. Note how it is the same as Equation 3, the equation for the buoyancy ratio. The model is only keeping track of the relative buoyancies.

Reference density $\bar{\rho}$ is the compositional density of the mantle. Christensen and Mooney (1995) calculated an modern average continental crust density of $2.8 \cdot 10^3$. Tenzer et al. (2015) provides seismically determined buoyancy ratios, which using Equation 11 and values in Table 1, can be used to calculate a modern oceanic crust density of $3.0 \cdot 10^3$. Note that the $\bar{\rho}$ used in this paper is significantly lower than the $\bar{\rho}$ that are found in similar papers (Mulyukova, 2015; Mulyukova et al., 2015; Todesco and Spera, 1992). This is because these other papers are using $\bar{\rho}$ for an average or lower mantle, which is under pressure and thus a significantly higher density. Our $\bar{\rho}$ was chosen to represent sub-crustal values.

Temperature has been nondimensionalized in the following way:

$$T' = \frac{T - 285}{\bar{\Delta T}} \quad (12)$$

Where T' and T are nondimensionalized and dimensionalized temperature and $\bar{\Delta T}$ is as found in Table 1. Taking 285 K and 3500 K as the temperatures at the top and bottom of the mantle, respectively, constrains all nondimensionalized temperatures in the model between 0 and 1.

Water fugacity has been nondimensionalized in the following way:

$$\begin{cases} f'_{H_2O} = 10 & \text{if } f_{H_2O} < 0.3 \\ f'_{H_2O} = 10^{(1-f_{H_2O})-1} & \text{otherwise} \end{cases} \quad (13)$$

where f'_{H_2O} and f_{H_2O} are nondimensionalized and dimensionalized water fugacity, respectively. The nondimensionalization of water fugacity has been represented by two different equations dependent on the water fugacity of the rock. This is due to hydrous and anhydrous rocks having different relationships to strain rates, as depicted in Figure 2

3.2 Numerical Methods

The following sections describe various numerical approximation methods that are utilized by the model, in addition to describing the amount of error that is accumulated by these approximations. Model figures in this section are from a numerical model coded in Python 3.7 and plotted using the matplotlib library. This model does not demonstrate thermochemical convection, but is still accurate in its depiction of the numerical methods.

3.2.1 Spatial Discretization

Continuous space cannot be stored by a computer, so modelers must get creative in their simulation of space. This model uses the finite element method in order to simulate a continuous 2D Cartesian plane, which conceptualizes space by using nodes, elements, and markers as explained below.

A node is a point in space, defined with Cartesian coordinates, where values such as temperature are known. Elements are defined by nodes and encompass the intervening space, where not all points are defined but the element can approximate values over that space. Nodes and elements occur in the rows and columns of a structured grid. The manner in which nodes define elements in this model is further elaborated in Section 3.3.3.

The fluid being simulated has its position and movement approximated using markers. Markers are mobile and can be advected through the model, unlike nodes or elements, therefore they can represent an evolving composition as they advect through space. However, it adds another source of error as information must be communicated from the grid to the markers and back, as discussed in 3.2.3. Markers can also define properties, such as temperature, density, viscosity, etc. The information that markers carry in this model is further elaborated in Section 3.3.5.

3.2.2 Advection

Markers in the model are advected, meaning the matter is transported while retaining its properties, such as density or temperature. The movement of advecting matter is described in equation 14, which states that the position vector of a point in space changes through time at the rate of its velocity vector.

$$\frac{\partial x_i}{\partial t} = v_i \quad (14)$$

x_i is a the position vector in the direction of i , t is time, and v_i is the velocity vector in the direction of i .

Continuous time, like continuous space, must be simulated through discretization. Equation 14 is approximated in the model using Euler's method as shown in equation 15, which can have varying orders of accuracy—this model uses first order accuracy, meaning it has terms up to the first derivative of the Taylor expansion as given in equation 16. The full Taylor expansion is a sum of infinite terms of derivatives evaluated at a point, which has full accuracy at that point. Using only terms to the first derivative introduces truncation error, which causes equation 15 to become less accurate further from the point of evaluation.

$$x_i(t + \Delta t) = x_i(t) + v_i \Delta t \quad (15)$$

$$x_i(t + \Delta t) = x_i(t) + \left. \frac{\partial x_i}{\partial t} \right|_{t=t_0} \Delta t + \left. \frac{\partial^2 x_i}{\partial t^2} \right|_{t=t_0} \Delta t^2 + \dots \quad (16)$$

x_i and v_i is a point's position or velocity in the direction of i , t is time, and Δt is time step.

The following scenario demonstrates how error can accumulate. Markers are advected with velocities determined by equations 17 and 18, which create n^2 convective cells.

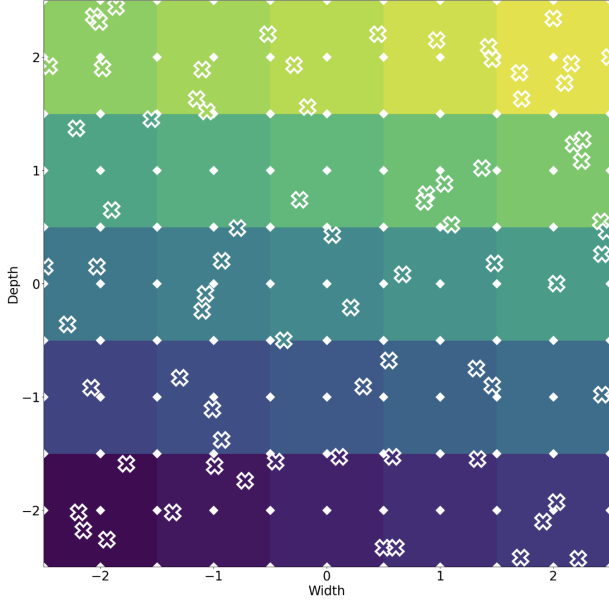


Figure 3: A plot showing a representation of elements, nodes, and markers. Nodes are represented as white diamonds. Elements are solidly colored in a color between purple and yellow to distinguish element boundaries. Markers are represented as x's with white borders to distinguish them.

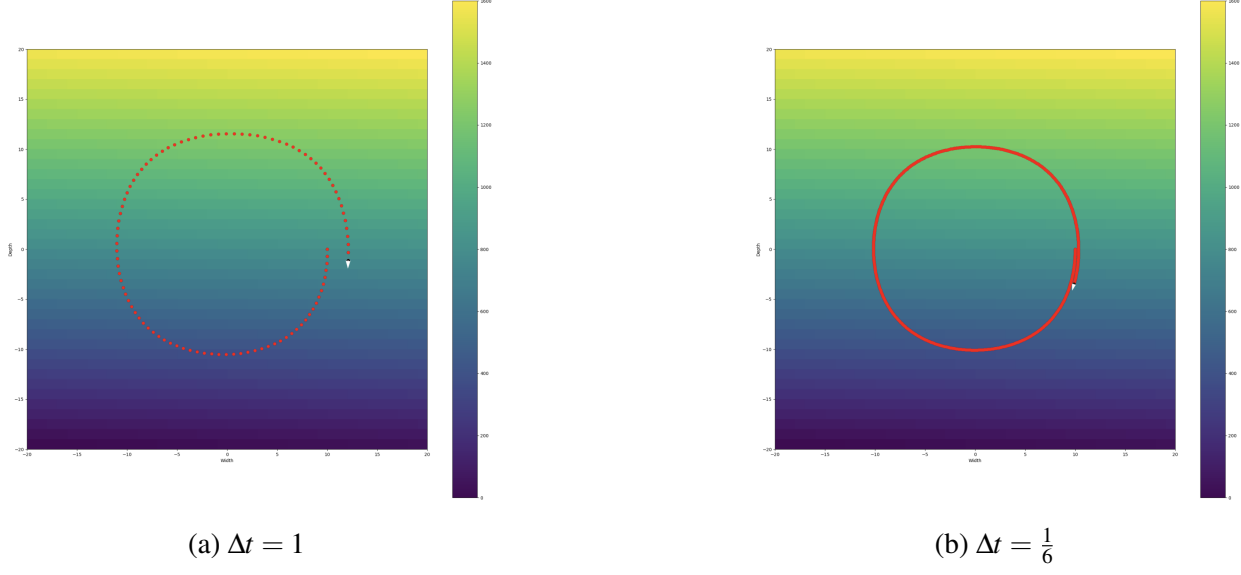


Figure 4: Both plots were generated at $n = 1$ and a resolution of 40. The velocity field is given by equations 17 and 18. The Marker is represented as a black point, and its velocity is represented as a white quiver, which was obtained through bilinear interpolation. It's previous positions are represented as red points. Note that (b) has smaller distances between previous positions, as a smaller amount of time has passed between steps.

$$V_x = |\vec{V}| \cos\left(\frac{n\pi x}{2L_x}\right) \sin\left(\frac{n\pi y}{2L_y}\right) \quad (17)$$

$$V_y = -|\vec{V}| \cos\left(\frac{n\pi x}{2L_x}\right) \sin\left(\frac{n\pi y}{2L_y}\right) \quad (18)$$

where V_x and V_y are velocities in the x and y directions, $|\vec{V}|$ is magnitude, n is the number of advecting cells, and L_x and L_y are the width and height of the model.

Markers are meant to be able to advect in a circle and pass through their initial starting points, but because they are moved along straight rather than curved lines, they will always pass to the outside of their starting points. This means that the error will accumulate, causing all markers to migrate away from the center of the convective cell. Figure 4 displays the observable difference in decreasing the size of Δt . This is more accurate due to the previously described truncation error for equation 15. Error increases as a function of distance from the point of evaluation. The Markers do not travel as far away from their ideal path before recalculating their velocity and adjusting their direction.

Figure 5 shows the benefit in increasing the number of elements, which is another way of increasing resolution. The number of steps and amount of time the simulation runs is different between the two plots, but proportional to each other such that time step for both plots is 1. Error decreases here because the initial evaluation of the point by equation 15 is more accurate in smaller elements, due to error introduced by bilinear interpolation (discussed in 3.2.3).

Figure 6 quantitatively describes how error relates to the resolution of the simulation. Each point was generated by a single simulation run with the indicated number of rows and columns (aspect ratio = 1) and a single marker generated in the same location as shown in Figures 5 or 4. The marker is allowed to advect in one full revolution, and the difference between where it should be and where it ended up is shown. In subfigure (a) the difference is shown in absolute units, which increases sharply before leveling off. In subfigure (b) the difference is shown proportional to the width of the simulation, which diminishes quickly before leveling off.

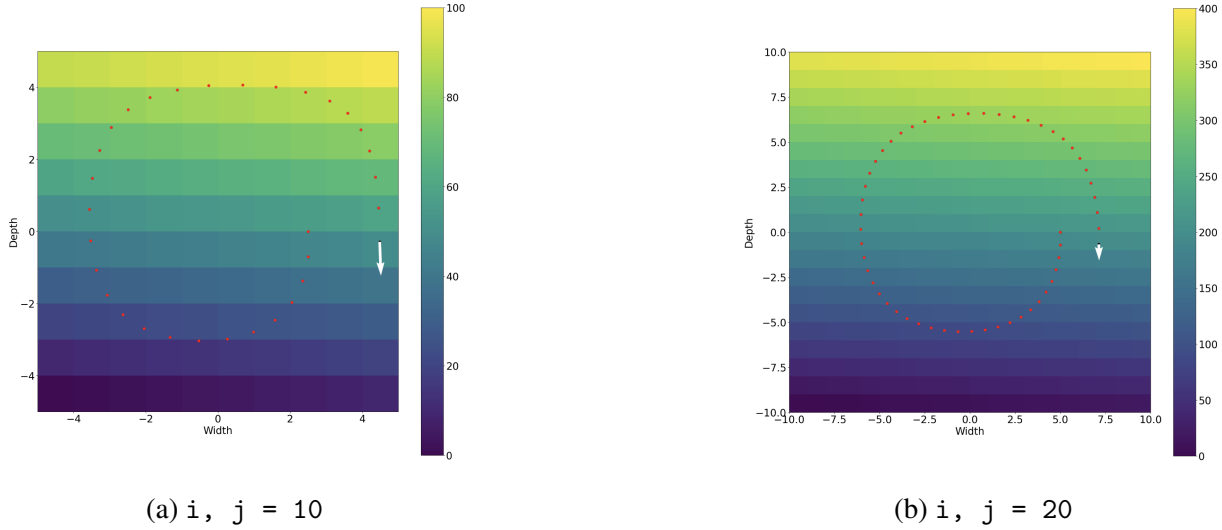


Figure 5: Both plots were generated using `Advection_Sim` with $n = 1$. The velocity field is given by equations 17 and 18. (a) used `time_end`, `num_steps` = 31, while (b) used `time_end`, `num_steps` = 53. This difference is to keep the same proportional time step while having the Marker complete roughly one revolution. The Marker is represented as a black point, and its velocity is represented as a white quiver, which was obtained through bilinear interpolation. It's previous positions are represented as red points.

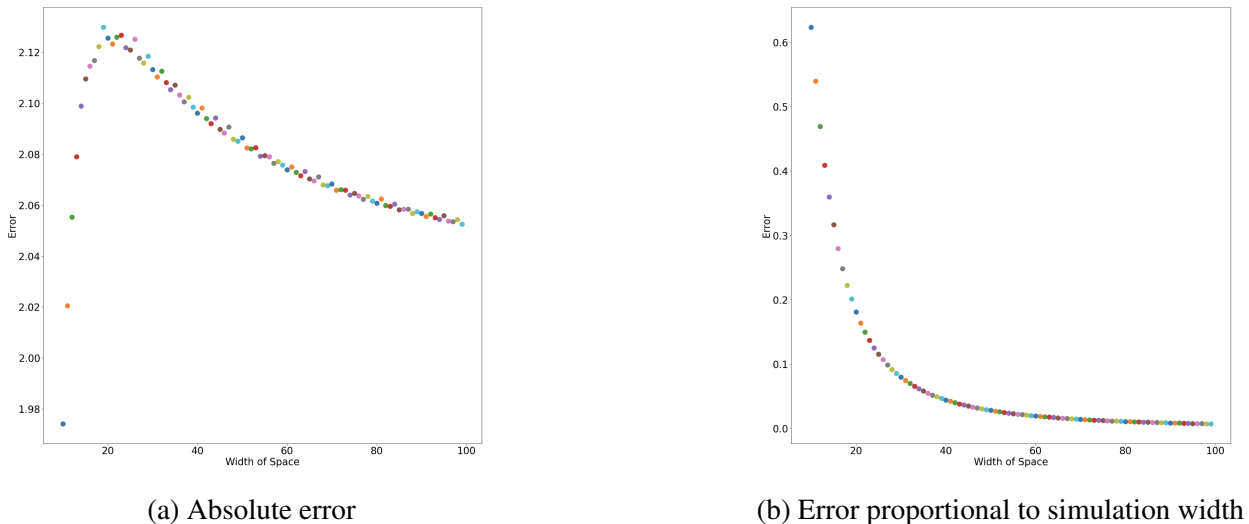


Figure 6: Two different conceptualizations of error accrued after one full revolution of a single Marker within a simulation. Error in (a) is defined as the difference between the Marker start and Marker end. Error in (b) is defined as the difference between Marker start and end squared, divided by the radius of the convective cell at 0° .

3.2.3 Interpolation

Marker velocities can be calculated using bilinear interpolation from the nodes of its containing element. The x and y velocities must be interpolated separately. For each value, it is first linearly interpolated in 1D along parallel sides of the box to create two intermediate points that lie on the same line as the target point. It is then linearly interpolated again using those intermediate values as the end points. Bilinear interpolation is defined by the below equations:

$$R_{1i} = Q_{11} \frac{x_2 - x}{x_2 - x_1} + Q_{21} \frac{x - x_1}{x_2 - x_1} \quad (19)$$

$$R_{2i} = Q_{21} \frac{x_2 - x}{x_2 - x_1} + Q_{22} \frac{x - x_1}{x_2 - x_1} \quad (20)$$

$$V_i = R_{1i} \frac{y_2 - y}{y_2 - y_1} + R_{2i} \frac{y - y_1}{y_2 - y_1} \quad (21)$$

where i is either x or y , R_{1i} and R_{2i} are intermediate velocity values, Q_{11} is the i velocity value for the bottom left node, Q_{21} is the i velocity value for the bottom right node, Q_{12} is the i velocity value for the top left node, Q_{22} is the i velocity value for the top right node, x_1 is the x coordinate for the left most nodes, x_2 is the x coordinate for the right most nodes, y_1 is the y coordinate for the bottom most nodes, y_2 is the y coordinate for the top most nodes, x and y are the coordinates of the target point, and V_i is the i velocity value for the target point. These values are also shown in Figure 7.

Interpolation can be visually demonstrated to show how marker velocities are derived from and relate node velocities. In Figures 8 and 9, the model was globally defined to have velocities set by equations 17 and 18. Node velocities are derived directly from equations 17 and 18, and marker velocities are bilinearly interpolated via the nodes of the containing element. Figure 8 demonstrates how marker velocities (represented as colors) are related to the surrounding nodes. Figure 9 demonstrates how close interpolation is to direct calculation. The markers and nodes are plotted over top of the field, but are very hard to see due to the similarity of the velocity's magnitude.

Figure 10 demonstrates how error can vary across different functions. Error is the difference between what the velocity field at a given location is based on the velocity equations, and what is calculated by interpolation. It is important to quantify so that it is known how far the model is from reality and how much error is accumulating over time.

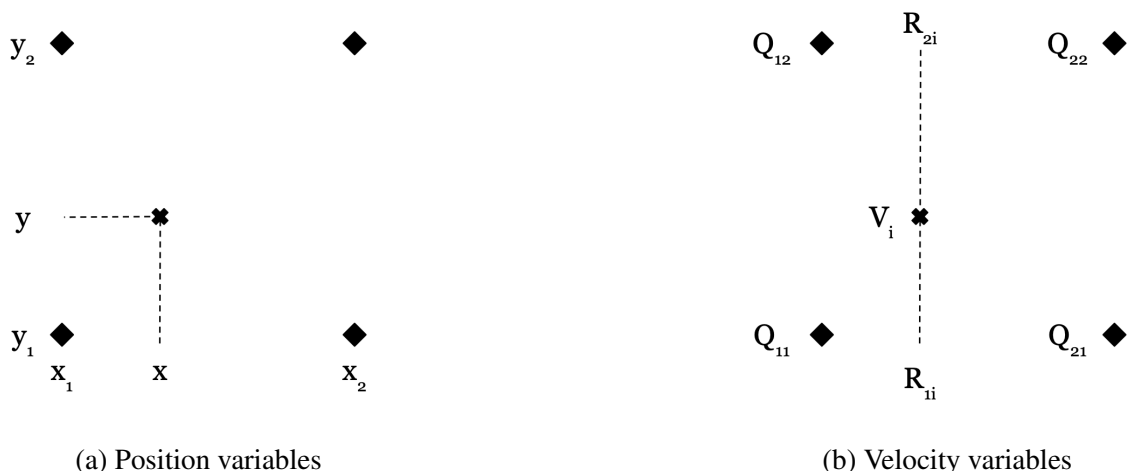


Figure 7: A depiction of the variables used in equations 19, 20, and 21. Nodes are depicted as black diamonds, the target point is depicted as an x.

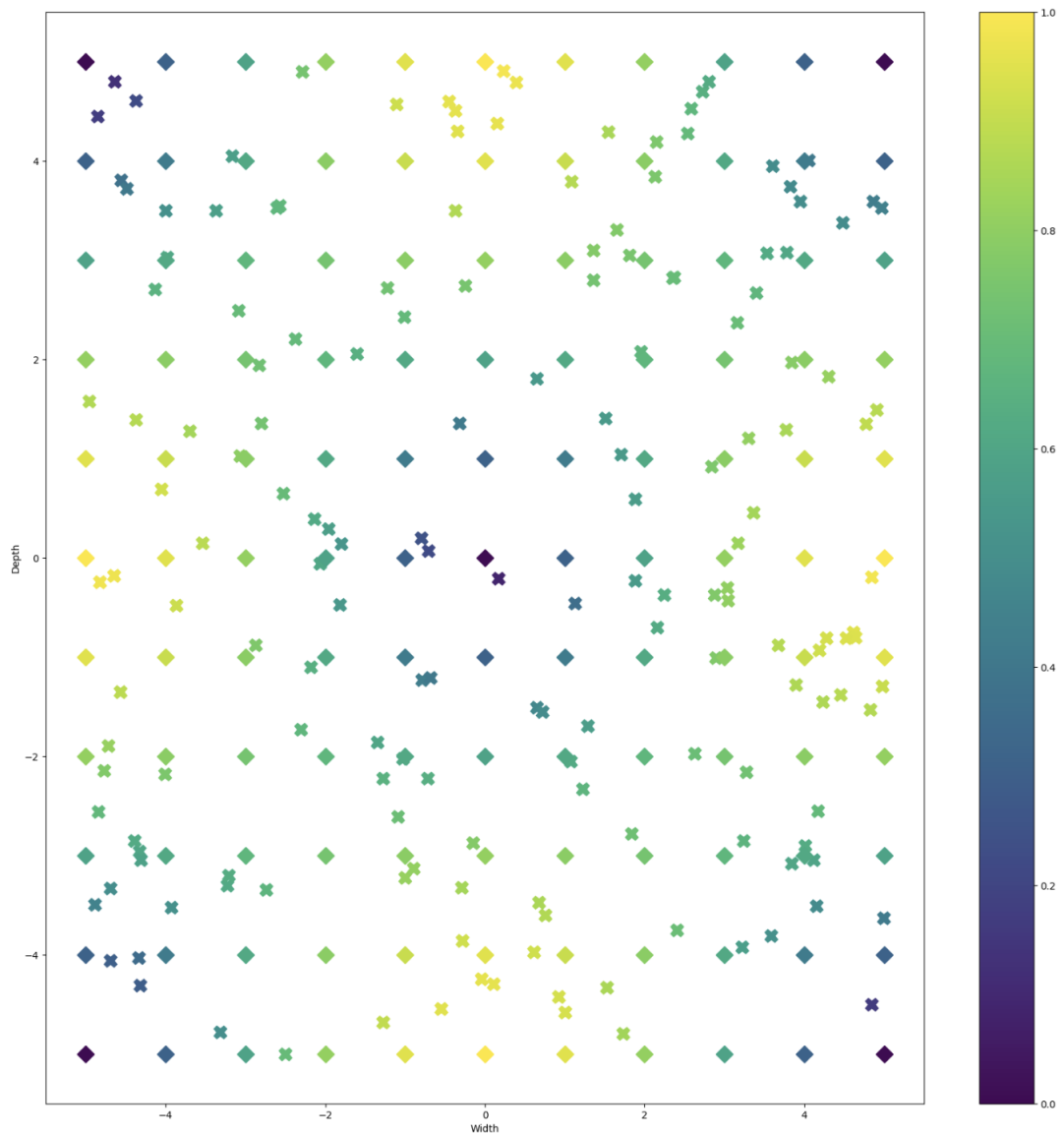


Figure 8: Nodes are depicted as diamonds and markers are depicted as x's. Node velocities are set by equations (17) and (18) and marker velocities are bilinearly interpolated. Purple represents a minimum velocity magnitude and yellow represents a maximum velocity magnitude.

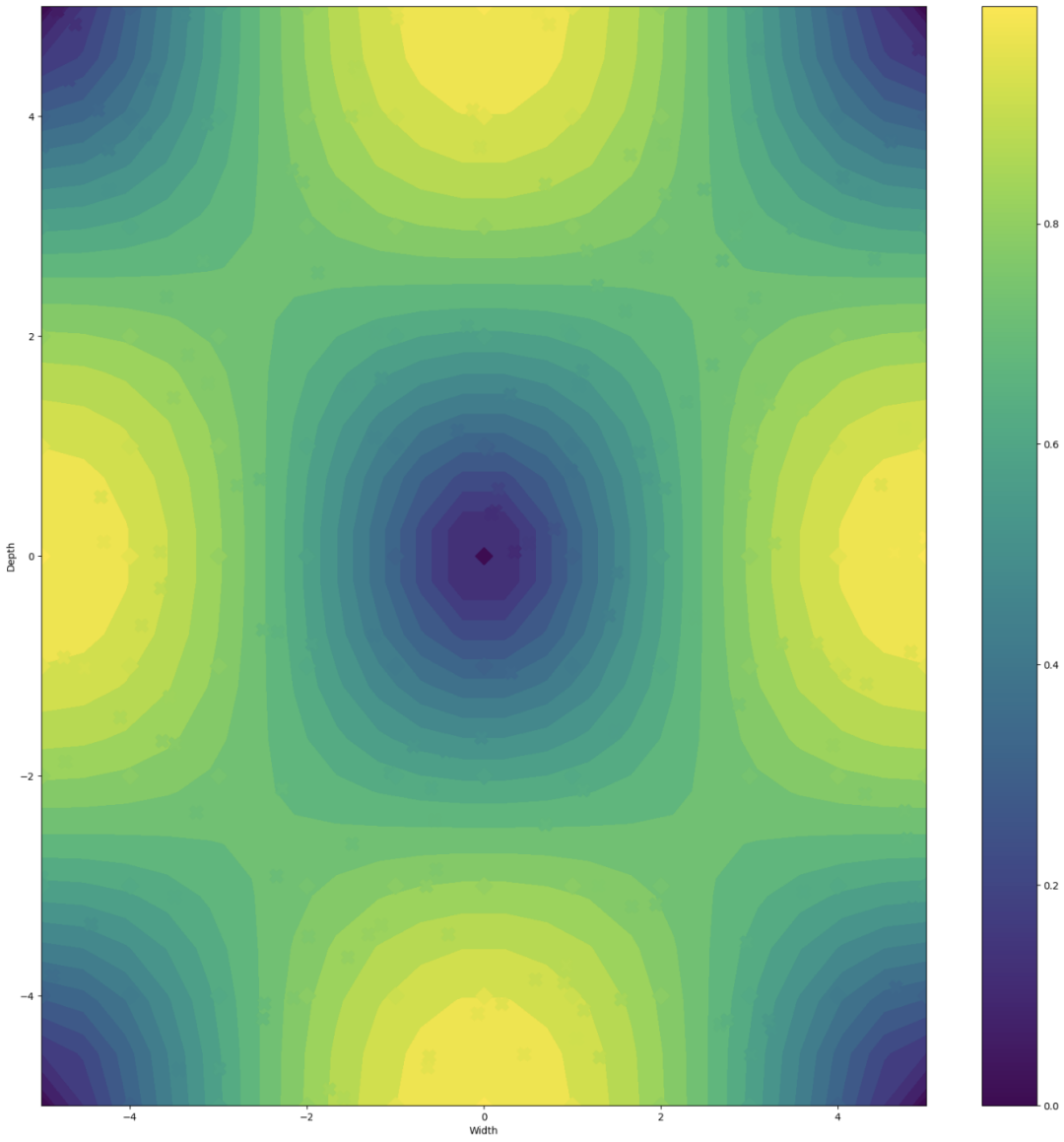
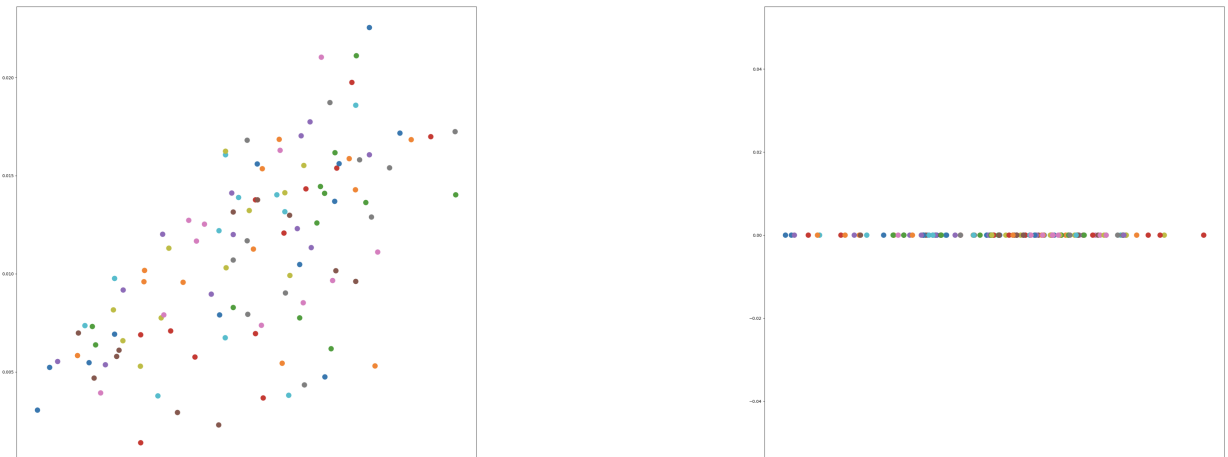


Figure 9: Nodes are depicted as diamonds and markers are depicted as x's. Node velocities are set by equations (17) and (18) and marker velocities are bilinearly interpolated. Purple represents a minimum velocity magnitude and yellow represents a maximum velocity magnitude. Markers and nodes are plotted on top of the velocity field, where each point is calculated from equations (17) and (18) (not interpolated). Magnitude difference between the velocity field and the markers is small, thus the markers are hard to distinguish.



(a) Error from bilinear interpolation in a velocity field generated from equations (17) and (18)

(b) Error from bilinear interpolation in a velocity field generated from a linear equation

Figure 10: The difference between (a) and (b) demonstrates how interpolation error can be different for different types of functions. Because bilinear interpolation assumes that the function is linear between nodes, there is no error with a linear function. There is a small but nonzero error with equations (17) and (18).

3.2.4 Gaussian Quadrature

In order to ensure the model adheres to the conservation of mass (the simulation does not lose or gain matter from nothing) and the conservation of momentum (the matter in the simulation does not gain or lose momentum from nowhere), the model weakly formulates these laws. Weak formulation demands that the integrated value of these quantities conserved over a finite domain, but not at all points within the domain. This is in contrast to strong formulation, which demands that the laws are conserved at every point in space.

In order to adhere to the weak formulation, the model approximates integrals over elements via Gaussian quadrature. Gaussian quadrature approximates an integral as a sum of weighted integration points, as shown in Equation 22.

$$\int_{-1}^1 f(x) dx \approx \sum_{i=0}^{N-1} f(x_i) w_i \quad (22)$$

In Equation 22, $f(x)$ is the function being evaluated over an interval of -1 to 1. N is the number of points that are used to approximate $f(x)$, which is chosen based on the degree of polynomial that is chosen to approximate $f(x)$. x_i is a predetermined point of evaluation, called an integration point, and w_i is the predetermined weight for that integration point, both of which are constant and can be looked up according to N . In essence, by evaluating the function at a few predetermined points and weighting them accordingly, the integral of that function over the given interval can be approximated.

Because it only approximates integrals occurring in the interval from -1 to 1, work is done beforehand in order to transpose the model's coordinate system into a local coordinate system where the approximation is done. This is done using equations 23 and 24.

$$x_m = o_{mx} + x_l \frac{\ell_{mx}}{\ell_{lx}} \quad (23)$$

$$y_m = o_{my} + y_l \frac{\ell_{my}}{\ell_{ly}} \quad (24)$$

x_m and y_m are the desired evaluation points in the model's coordinate system. x_l and y_l are the given evaluation points in the -1 to 1 interval. ℓ_m is the length or width of the element, and ℓ_l is the length or width of the integral range, which here is always 2. o_m is the origin of the evaluated region, which here is the center of the integrated element and described further in 25 and 26.

$$o_{mx} = x_{11} + \frac{x_{21} - x_{11}}{2} \quad (25)$$

$$o_{my} = y_{11} + \frac{y_{12} - y_{11}}{2} \quad (26)$$

x_{11} and y_{11} are the coordinates of the bottom left node, x_{21} is the x coordinate of the bottom right node, and y_{12} is the y coordinate of the top left node. The variables in equations 23, 24, 25, and 26 are all pictured in Figure 11.

If the function being approximated is a polynomial of degree $2N - 1$ or less, it can be approximated exactly with Gaussian quadrature. Because equations 1 and 5 are not polynomials, there is an error associated with our approximation. Figure 12 shows a comparison of error generated by the quadrature for a polynomial versus a sinusoidal function. Because points were evaluated directly and not from bilinear interpolation, error from Gaussian quadrature is the only error present in the integration plots.

When practically used in the model, Gaussian quadrature will be used in conjunction with interpolation. In Figure 13, a density field is prescribed globally and at the nodes. Then the quadrature is conducted across every element, where evaluation points are determined and then evaluated by interpolating the density values assigned at the nodes, as if the evaluation point were a marker. The figure shows the large potential error from combining Gaussian quadrature with bilinear interpolation. Note the difference in scale axis—(b) has a max of .15 while (a) only has a max of .0004. If they were plotted with the same axis, (a) would appear to have no error.

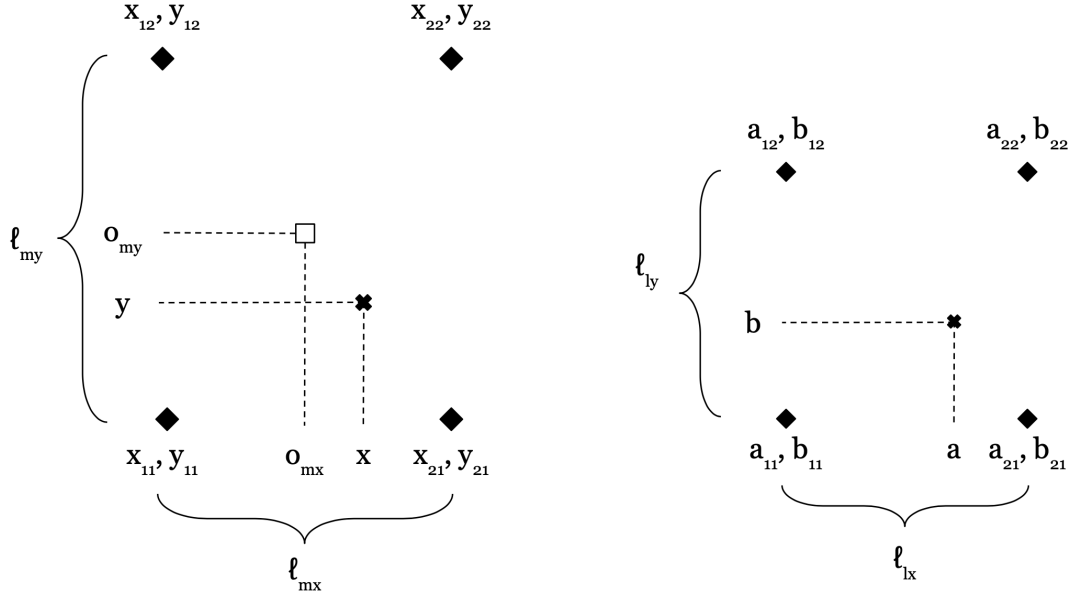


Figure 11: A depiction of the variables used in equations 23, 24, 25, and 26. The left element is the model element and the right element is the integral range, which is always -1 to 1. Nodes are depicted as black diamonds, the target point is depicted as an x, and the origin of the model region is depicted as a hollow black square.

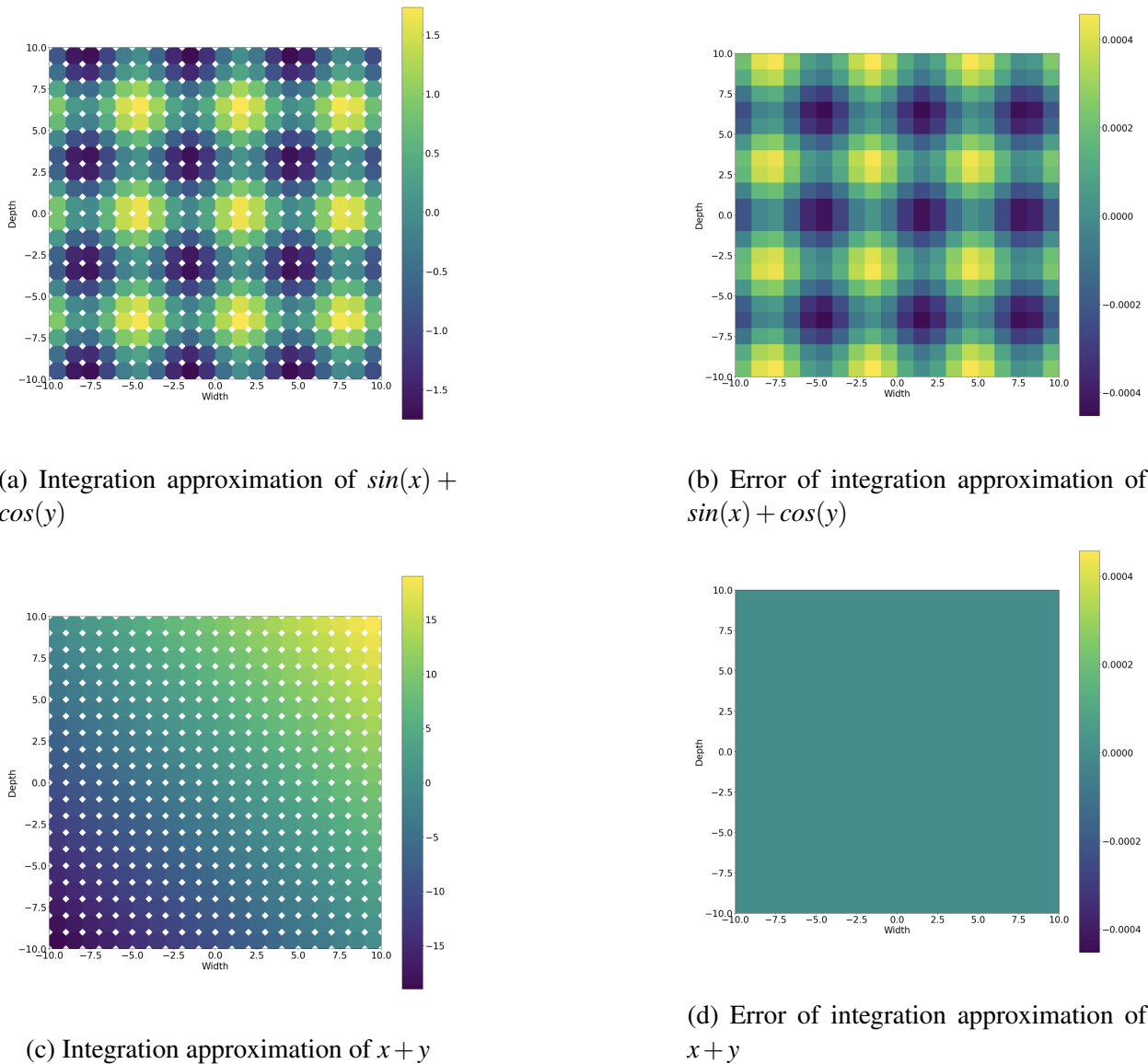


Figure 12: (a) and (c) are both plots of Gaussian quadrature of a space generated by Space(20, 20), where nodes are represented as white diamonds. (a) integrates over a globally prescribed field of $\sin(x) + \cos(y)$. (c) integrates over a globally prescribed field of $x + y$. Evaluation points were calculated directly from global fields. (b) is an error plot between the quadrature of (a) and the mathematically exact integral of the global field over each element. (d) is an error plot of the same nature for (c). (b) and (d) use the same color scale. Run using `Gauss_error()`.

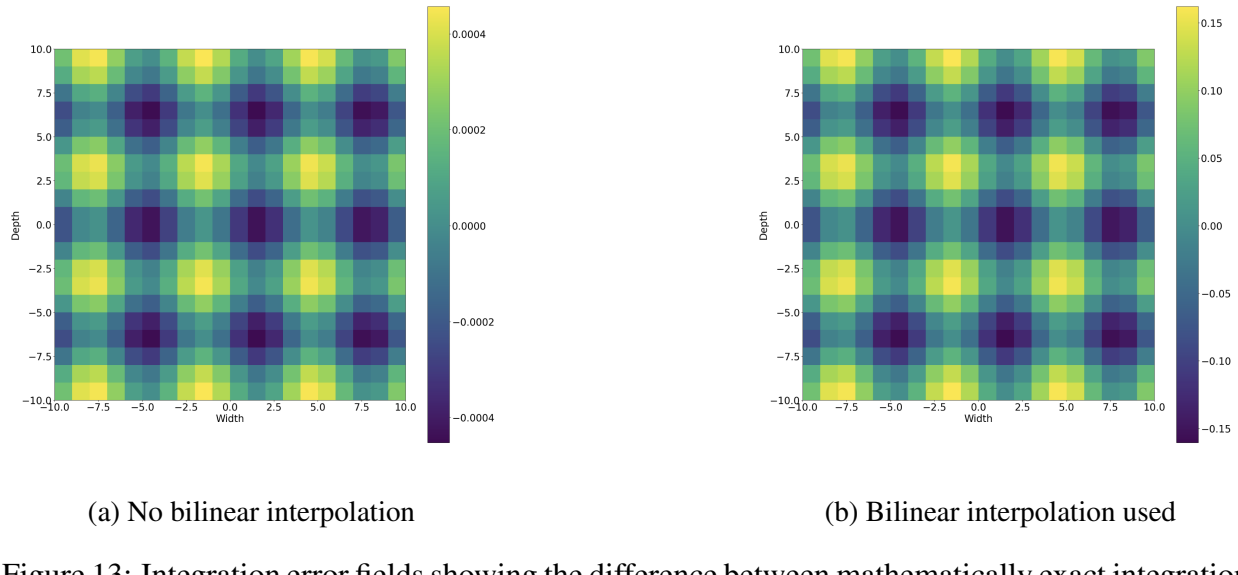


Figure 13: Integration error fields showing the difference between mathematically exact integration and that calculated by Gaussian quadrature. In (a), evaluation points are calculated directly from $\sin(x) + \cos(y)$. In (b), the evaluation points are bilinearly interpolated. Note difference in axis measurements.

3.3 MATLAB Model Design

The model that will be used in order to acquire results is written in MATLAB and modified from (Mulyukova, 2015). This model utilizes all of the numerical methods described in 3.2. Space is discretized using the nodes and elements scheme described in Section 3.2.1. Markers are advected as described in Section 3.2.2. Values are interpolated and exhibit the error described in Section 3.2.3. Values are integrated using quadrature described in Section 3.2.4.

3.3.1 Initialization and Loop Steps

The model starts by initializing parameters that will be modified by the simulation. The initialization steps are defined below and further elaborated in the next sections:

1. Define model parameters (ρ, μ, f_{H_2O}, D , etc) (Section 3.3.2)
2. Spatial discretization and model geometry: Define elements, nodes, aspect ratio (Section 3.3.3)
3. Initialize vaules at markers: $\rho, H_2O, H, n_{melt}, t_{melt}$ (Section 3.3.5)
4. Initialize values at nodes: ρ, H_2O, H, T, μ (Section 3.3.6)
5. Temporal discretization: Δt set (Section 3.3.4)
6. Save variables: Ra, Br, μ , ρ , D_{melt} , etc. (Section 3.3.10)

Once the model has been set up, it is ready to evolve. It undergoes the following steps each time step:

1. Thermal solver (thermal diffusion): addresses the diffusion component of Equation 5 (Section 3.3.7)
2. Mechanical solver: calculates velocities at the nodes (Section 3.3.8)
3. Mechanical advection/Reseeding: advects markers and may undergo a reseeding routine (Section 3.3.8 and Section 3.3.9)
4. Thermal advection: addresses the advection component of Equation 5 (Section 3.3.7)
5. Melt markers: update marker composition (Section 3.3.5)
6. Update values at nodes: communicate information from markers to nodes (Section 3.3.6)
7. Update time: move forward simulation and recalculate Δt (Section 3.3.4)
8. Save variables: ρ, μ, H_2O, H, T, t (Section 3.3.10)

3.3.2 Model Parameters

Many of the variables described in Table 1 are parameters that are purposefully not deviated from their reference values in order to explore possible outcomes, such as ρ . There are also parameters the model defines that are not covered in Table 1. Below is a list of the parameters I plan to vary:

- ρ_{min} (minimum possible density) and ρ_{inc} (the amount ρ increases by when it melts).
- f_{H_2OM} (initial water fugacity of mantle) and f_{H_2Oinc} (the amount f_{H_2O} decreases by when it melts).
- H_M (activation enthalpy of mantle), H_{max} (maximum possible activation enthalpy), and H_{inc} (the amount H increases by when it melts).
- D_{melt} (the depth at which melting occurs).

3.3.3 Spatial Discretization and Model Geometry

The spatial discretization of this model is similar to the methodology described in 3.2.1. A continuous 2D Cartesian plane is simulated through sets of nodes, elements, and markers. Elements and nodes make up a structured grid. This model has two different resolutions of element meshes. Mechanical elements are defined by 9 nodes in a 3 by 3 configuration. Thermal elements are defined by 4 nodes with each node at a corner. Mechanical elements contain 4 thermal elements. The mechanical and thermal meshes use the same nodes.

Mechanical elements are used for integration in solution to the Stokes equation, while thermal elements are used for integration in the solution to the thermal equation. Because solving the Stokes equation requires finding higher order derivatives, it requires elements with more nodes than the thermal solver.

The top and bottom boundaries of the box are defined to maintain certain characteristics throughout the run of the model. For the mechanical solution, the markers are not allowed to leave the box, so markers along these boundaries are given a vertical velocity of 0. Markers that would leave the box based on their velocity are instead placed at the boundary. For the thermal solution, the top and the bottom boundaries maintain the temperature they were assigned at the initialization of the model.

The model is defined to have rectangular geometry. This introduces error because it simulates the mantle as having as much contact with the outer core, which heats it, as it has surface from which it cools. It also necessitates the definition of lateral boundary conditions in the model, whereas the mantle has no lateral boundaries. For the mechanical solution, the lateral boundaries also do not allow markers to escape the box, and their horizontal velocity is set to 0.

Melting depth D_{melt} is adjusted to accommodate the resolution of the model in this section as well. During the reseeding process (described in Section 3.3.9), it is possible for 'melted' markers to be placed below the melting depth if D_{melt} does not coincide with element boundaries, which results in erroneously melted markers. Therefore, D_{melt} is shifted to the nearest element boundary.

3.3.4 Temporal Discretization

In order to advect markers, time must be discretized as shown in Equation 15, where time t is some current time and there is some Δt that defines the amount of time between now and the next time step. During initialization, time $t = 0$ and Δt is given an initial value.

At the end of the loop, t is incremented by the previously defined dt and is then recalculated with equation 27.

$$\Delta t = 4 \cdot \min \left(dx ./ \sqrt{V_x^2 + V_y^2} \right) \quad (27)$$

$$dx = \frac{4 \cdot L_1 \cdot L_2}{n_{el}} \quad (28)$$

Where Δt is time step, V_x a matrix of all horizontal node velocities, V_y a matrix of all vertical node velocities, L_1 and L_2 the horizontal and vertical extents of the box, respectively, and n_{el} the number of elements.

This is done so that the time step is proportional to the velocity, in order to limit advection error described in [3.2.2](#) while still being computationally efficient.

3.3.5 Markers

The number of markers in the vertical direction is defined as $c \cdot n_{el}$, where c is an even integer and n_{el} is the number of elements in the vertical direction. The number of markers in the horizontal direction is defined as $n_{mv} \cdot a$, where n_{mv} is the number of markers in the vertical direction and a is the aspect ratio of the box.

Markers are initialized with the following attributes:

- ρ (density)
- f_{H_2O} (water fugacity)
- H (activation enthalpy)
- n_{melt} (the number of times the marker has melted)
- t_{melt} (the most recent time the marker has melted)

They are all initialized with mantle values, except for those that are already within the melt region. Those that are already within the melt region undergo a melting event during initialization. During the time loop, markers may also undergo melting events.

A melting event occurs when a marker advects above the melting depth D_{melt} . Markers only melt when they cross into this region, not when they leave it. When markers melt, ρ , f_{H_2O} , and H increase/decrease by ρ_{inc} , f_{H_2Oinc} , and H_{inc} respectively, as long as it would not put them above/below ρ_{min} , f_{H_2Omin} , or H_{max} . n_{melt} increases by 1, and t_{melt} is updated to match the current time t .

After melting events are resolved, both in initialization and in the time loop, information is communicated from the markers to the nodes. Nodes receive a value based on the markers in the elements that the node is a part of. Markers are weighted the same way that integration points are in [3.2.4](#) as a function of distance from the node.

3.3.6 Nodes

Node positions are first initialized as described in Section [3.3.3](#). They are then initialized for other values:

- ρ (density)
- f_{H_2O} (water fugacity)
- H (activation enthalpy)
- T (temperature)
- μ (viscosity)

ρ , f_{H_2O} and H in the nodes solely receive their values from markers, as described in Section [3.3.5](#), and are utilized in the mechanical solver and/or the reseeding process described in Sections [3.3.8](#) and [3.3.9](#), respectively.

Temperature in the nodes is initialized according to the prescribed temperatures of the bottom and top of the mantle. They are set to $0.5 \cdot \Delta T - r$ where r is a very small random number in order to help convection initiate. Small variations help the mechanical solver hone in on one solution. Temperature in the nodes is updated every time step by the thermal solver described in Section [3.3.7](#).

As discussed in Section [3.1.3](#), viscosity is controlled by temperature, water fugacity, and activation enthalpy in this model. Notice that Equation [7](#) does not directly account for the effect of pressure or mineral structure on viscosity, the importance of which is described in Section [2](#). In order to account for this, nodes are prescribed a μ_z according to their depth so that the combination of μ_z and the model calculated effect of temperature produce a more realistic viscosity profile, as shown in Equation [29](#).

$$\mu' = \mu_z \cdot \mu'(T', f'_{H_2O}, H) \quad (29)$$

$$\mu'(T', f'_{H_2O}, H) = \mu_0 \cdot f_{H_2O} \cdot \exp\left(\frac{H}{CRT}\right) \quad (30)$$

$$\mu_0 = \exp\left(\frac{-H}{BRT_t}\right) \quad (31)$$

μ' is nondimensionalized viscosity, μ_z is viscosity attributed to depth, T' and T are nondimensionalized and dimensionalized temperature, T_t is temperature at the upper boundary of the mantle, f'_{H_2O} and f_{H_2O} are nondimensionalized and dimensionalized water fugacity, H is activation energy, R is the gas law constant, and C and B are scaling constants where $B > C$.

Figure 14 displays the relationship between viscosity, temperature, and water fugacity in the model, as described in Equation 30. Viscosity has an exponential relationship with temperature, becoming stiffer at lower temperatures. Viscosity is also dependent on water fugacity and activation enthalpy, as described in Section 2. In the model, water fugacity and activation enthalpy evolve in lockstep, as described in Section 3.3.5. As the markers melt, they decrease in water fugacity and increase in activation enthalpy; this modifies the range of possible viscosity values. In Figure 14, bands of similar color correlate to a similar water fugacity, showing how a higher water fugacity correlates to a lower viscosity for all temperatures, but that the effect of water fugacity is still secondary to the effect of temperature.

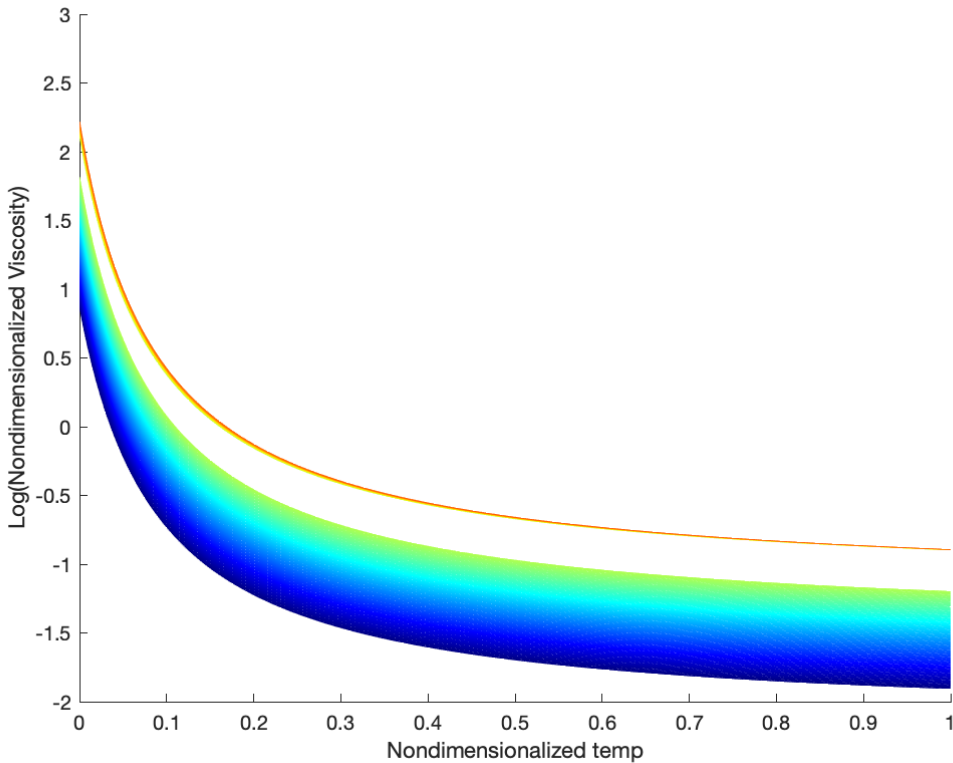


Figure 14: A plot of log(viscosity) versus temperature, both nondimensionalized. Bands of same color are values of the same water fugacity. Orange values are low water fugacity (nondimensionalized 0) and high activation enthalpy (370), dark blue values are high water fugacity (nondimensionalized 1) and low activation enthalpy (330).

3.3.7 Thermal Solver

The first thing in the loop is the thermal diffusion solver, which integrates over all thermal elements in order to solve for temperature (Equation 5) at every node. The error introduced by this integration is described in 3.2.4. The thermal solution adheres to the boundary conditions set in 3.3.3. At this point, the thermal solution only accounts for thermal diffusion because the material has not been advected yet. It is only part of the solution to equation 5, as described in Section 3.1.2.

Thermal advection occurs later, where a full solution to equation 5 is found for temperature in the nodes. In addition to thermal diffusion, the temperature at a given point in space is determined by the temperature of the material that has been advected into that location. Velocity at the nodes is known because thermal advection occurs after a solution to the Stokes equation (Equation 1) is

found, and while the material has been advected, the temperature has not. The velocity at each node can be used to determine the position of that material's position at the previous time step. That point where the material is coming from is called the feet of the characteristics. Note that the temperature at the feet are already diffused. Temperature for the feet of the characteristics is interpolated from the nodes of the element the feet are in. That gives a solution for temperature in the nodes.

3.3.8 Mechanical Solver

The mechanical solver integrates over all mechanical elements (error described in [3.2.4](#)) in order to solve equation 1 for the vertical and horizontal velocity at every node. The mechanical solution adheres to the boundary conditions set forth in [3.3.3](#).

It is then possible to advect the markers, where they are moved according to equation 15. Marker velocities are interpolated from node velocities calculated in the previous step, introducing error described in [3.2.3](#). This is when a reseeding process may occur, if there are any thermal elements with no markers inside of it, which may occur due to the advection error described in section [3.2.2](#). This is necessary to prevent errors when updating thermal elements according to the values of their markers. The solution of reseeding, instead of looking at markers in nearby elements, limits error in underrepresented areas by ensuring the distance between the points used for interpolation and the point being interpolated remains small, but introduces a small amount of error everywhere due re-interpolating all marker values (error described in Section [3.2.3](#).)

3.3.9 Reseeding Routine

Reseeding first moves all markers back to their original positions so that there are markers in all thermal elements. It then generates a temporary ultrafine mesh with as many elements as markers in vertical direction as prescribed during initialization (see [3.3.3](#)). New markers are generated in the centers of these elements. The reseeding process attempts to limit the error introduced by interpolation by using the previous marker values where possible, and only interpolating from node values when the ultrafine mesh elements are empty. All markers are then readvected and the loop continues.

3.3.10 Save Variables

The last thing that occurs during the initialization stage of the model is saving all of the variables that will be constant throughout the model run in order to plot data afterwards. This includes Ra , Br , μ , ρ , D_{melt} , the length of time the simulation will run for, how often the model should save dynamic variables, the aspect ratio of the box, the number of mechanical elements in the vertical direction, and the depth of the box.

The last thing that occurs within the loop is saving all of the values necessary for later plotting: all marker values, the temperature in the nodes, the density of the nodes, the viscosity in the nodes, the activation energy in the nodes, the horizontal and vertical velocity in the nodes, and the total simulation time. They are only saved after some specified amount of simulation time has passed in order to be more computationally efficient.

3.4 Quantification and Measurement of Results

The model seeks to understand how varying parameters such as water fugacity, activation enthalpy, melting depth, and chemical buoyancy difference will affect continent formation. Therefore, the model must be able to quantify and measure formational changes between model runs. The model will do this by looking at differences in mantle mixing rates, crustal building rates, continental mass, etc.

3.4.1 Rate of Crustal Building

At each time step, the number of times each marker has melted is known. A proxy for the rate of crustal building can be constructed by looking at the difference in the number of marker melt events between adjacent time steps, as all crust must have undergone at least one melting event. This assumes that markers have mass, which is inaccurate. Markers have a density, so higher or lower concentrations of markers within the same region with the same density will not change the

mass. However, higher amounts of markers that have melted more times may relate to a higher number of elements with a lower density, which does result in a different mass.

3.4.2 Rate of Mantle Mixing

At simulation start, there are no markers that have undergone a melting event that are below the melting depth. Each element can keep track of the first time they saw a marker that has melted at least once. It can track rate of mantle mixing, and it can also reveal if there are areas that do not participate in mixing and have remained primitive.

3.4.3 Crustal Reworking

Continental formation involves the reworking of surface material and the increased concentration of silica in continental crust. The model simulates this by keeping track of the number of times each marker has melted (n_{melt}) and updating the density, water fugacity, and activation enthalpy of the marker each time it is melted.

This allows the following metrics to be tracked:

- Amount of time it takes for a given marker to have melted a certain number of times. This would give insight into the rate of crustal reworking.
- Look at the percent breakdown of the area above the melt region over time. Looks at changing chemical composition of crust over time.
- Is there a n_{melt} that is buoyant enough that it does not get entrained in subduction?

4 Results

4.0.1 Base Cases

For the following runs, viscosity is not calculated according to Equation 29 and has no dependence on temperature, water fugacity, or activation enthalpy; it is set to a uniform value. The number of times a marker could melt was limited to one.

The current results were run for the following scenarios:

- No contrast (Figure 15): $Br = 0, \Delta\mu = 0$
- μ contrast (Figure 16): $Br = 0, \Delta\mu = 10$
- ρ contrast (Figures 17 and 18): $Br = -0.5, \Delta\mu = 0$

Aside, they all had the same properties. The markers that have undergone a melting event represented by black dots in the figures. None of the methods described in 3.4 were implemented at the time these simulations were run, but they can still be visually examined in order to qualify differences in continental mass and shape caused by the variations set between model runs.

The no contrast run can be taken as a baseline, from which the μ contrast and ρ contrast runs deviate from due to their single parameter variation. Because there is no physical difference between crust (has undergone a melting event) and mantle (has not undergone a melting event) in this run, the markers freely convect, migrating from the top of the box to the bottom and again to the top. This is as expected with $Br = 0$ (purely thermal convection). The crustal markers make nearly three full revolutions around the box. Starting around $t = 0.02$, some minor downwelling begins along the top of the mantle inside of the established convective cell. The crust that is visibly perturbing from this is entrained downwards before it is able to downwell, and the lumpy structure is preserved. When it reaches the bottom, it grows slightly larger as that material travels a further distance due to having migrated closer to the center of the convective cell than the material on the outside, that has further to travel. Several more of these lumps appear over the course of the simulation.

In μ contrast, there is a noticeable difference from the no contrast run. The crust is 10 times more viscous than the mantle. It is still a purely thermal convection, so the markers still migrate around the edges of the box with the convective flow, but it is a much more slow and laminar flow. In the same time that the crustal markers complete nearly three revolutions of the box in the no contrast

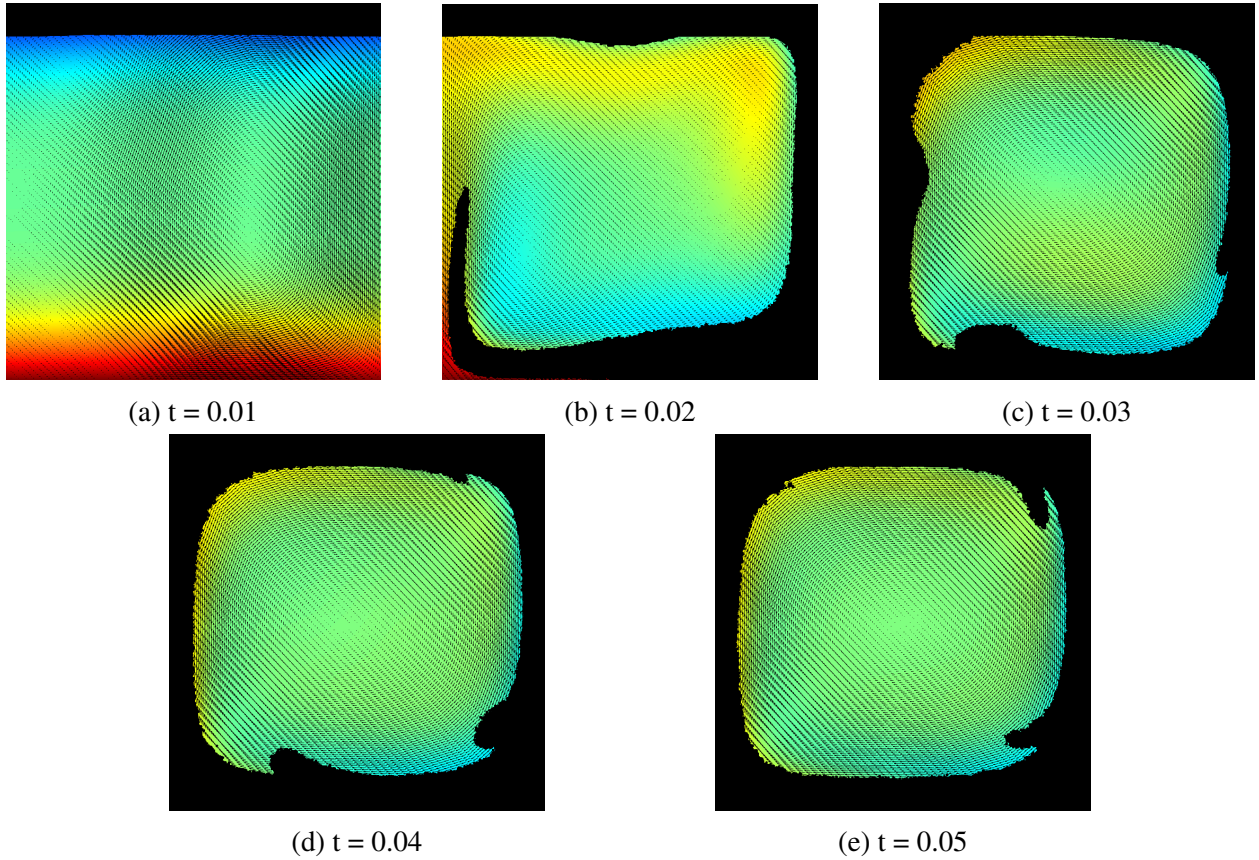


Figure 15: No contrast case. Snapshots of model run with the following parameters: $\text{Ra} = 10^5$, $\text{Br} = 0$, $\rho = [0, 0]$, $\mu = [1, 1]$, melt region = 50/600, $n_{el} = 100$. The velocity field is depicted with small black arrows in the direction of the velocity vector at that point. The temperature is depicted as a colored gradient from blue (cold) to red (hot). $n_{melt} = 1$ markers (crustal markers) are depicted as black dots.

case, they do not complete one in the μ contrast case. The higher viscosity of the crust also means that it does not form the lumps that were seen in the no contrast case.

ρ contrast is the most visually different. The crust resists the downward entrainment of the convective flow. The initial large cold downwelling entrains the most of the material, but as the plume disperses and the mass becomes warmer, it becomes buoyant enough to rebound and rise towards the surface. Meanwhile, mantle material is still rising in hot plumes towards the surface and is melting into anomalous crust. Because the cold material is not participating in the convective cell due to its chemically induced buoyancy, it begins to grow in size, as seen in both Figures 17 and 18, which shows the compositionally anomalous mass and the cold mass respectively. By $t = 0.04$, the cold mass forms its own convective cell as it is still underlain by warmer material. Some crustal material is entrained by the mantle convective flow, but it meets a rising plume from underneath the cold mass that drives the entrained markers upwards again. The rising hot plume creates a second mantle convection cell. The material at the edge of the anomalous crust mass is then experiencing the convective stresses of both mantle convection cells, and some crustal material is entrained in the smaller convective cell. This is partially visible in Figure 18, but much more visible in Figure 17. Similar to the no contrast case, and very unlike the μ contrast case, the viscosity is low enough that thin structures are created and preserved.

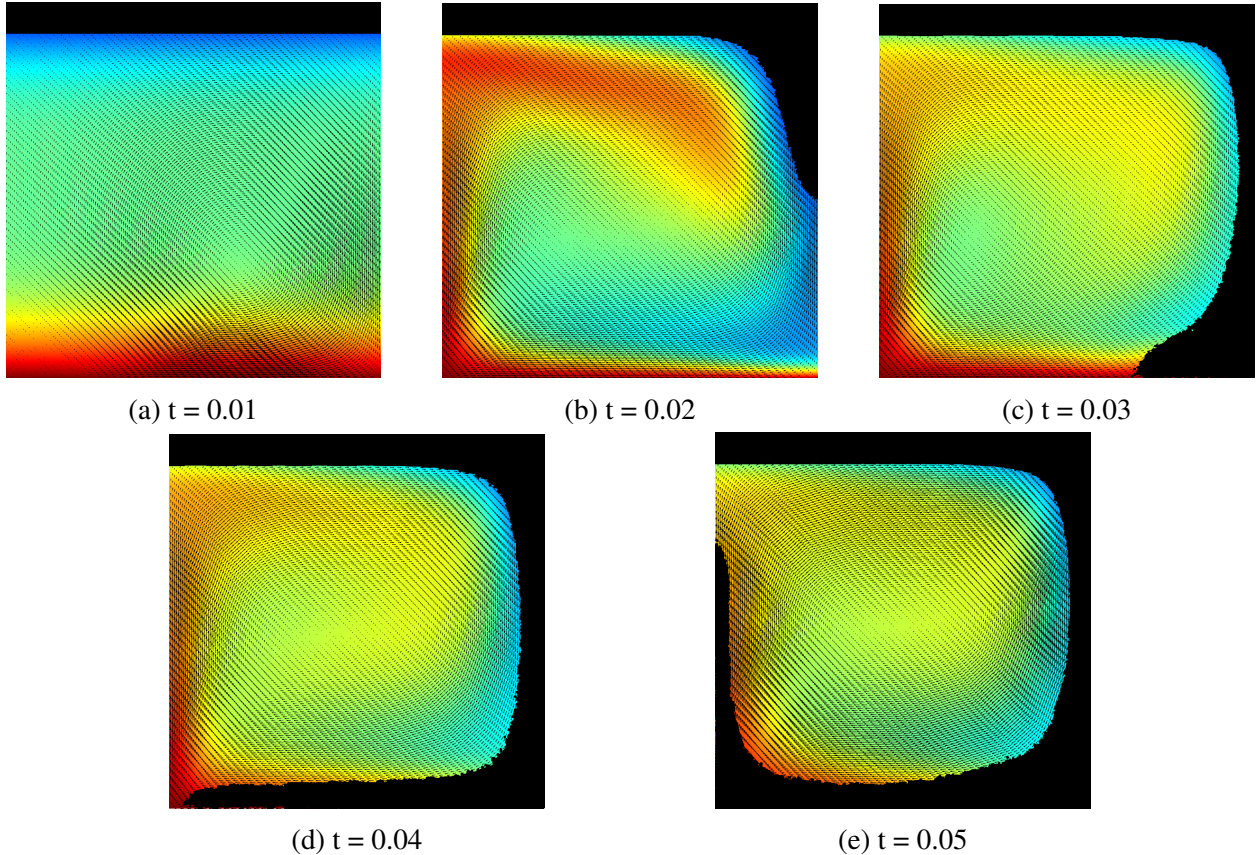


Figure 16: μ contrast case. Snapshots of model run with the following parameters: $\text{Ra} = 10^5$, $\text{Br} = 0$, $\rho = [0, 0]$, $\mu = [10, 1]$, melt region = 50/600, $n_{el} = 100$. The velocity field is depicted with small black arrows in the direction of the velocity vector at that point. The temperature is depicted as a colored gradient from blue (cold) to red (hot). $n_{melt} = 1$ markers (crustal markers) are depicted as black dots.

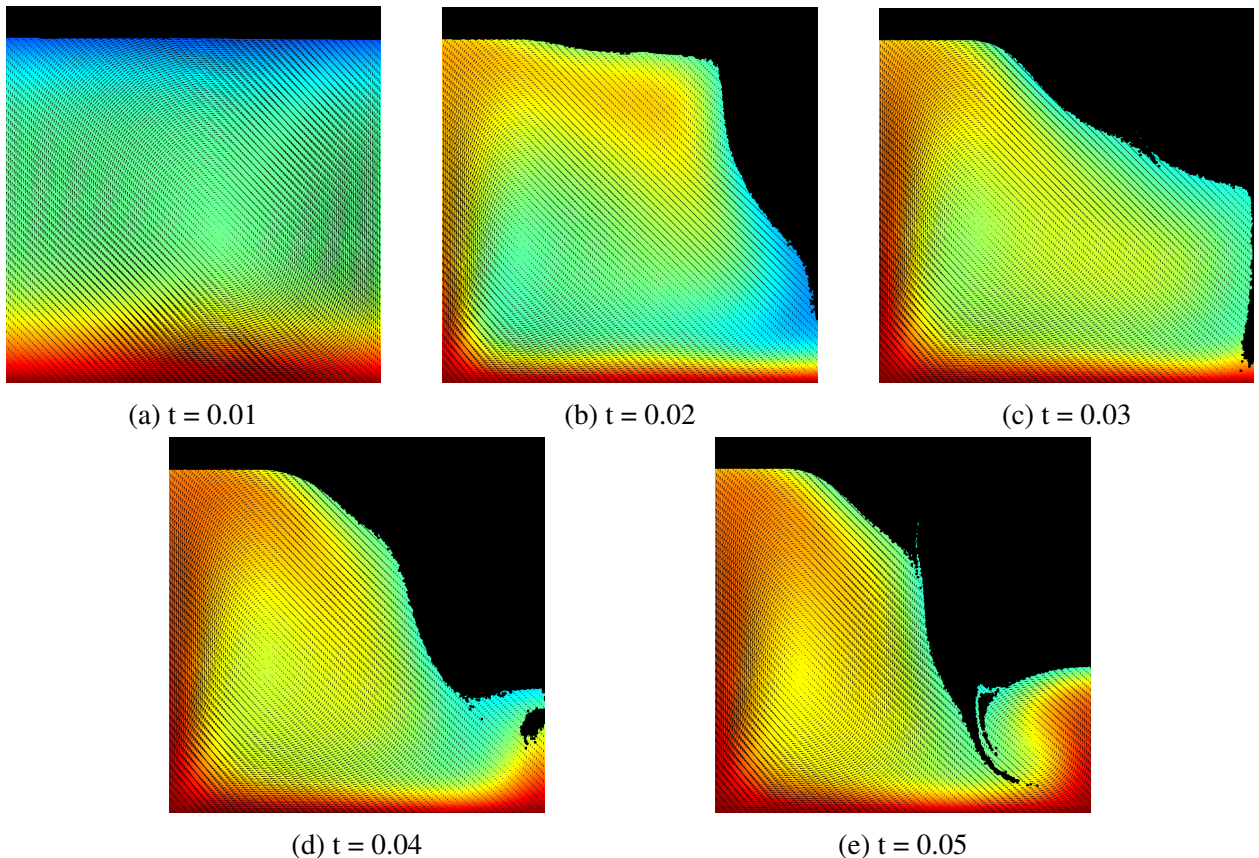


Figure 17: ρ contrast case. Snapshots of model run with the following parameters: $\text{Ra} = 10^5$, $\text{Br} = -0.5$, $\rho = [\text{Br}, 0]$, $\mu = [1, 1]$, melt region = 50/600, $n_{el} = 100$. The velocity field is depicted with small black arrows in the direction of the velocity vector at that point. The temperature is depicted as a colored gradient from blue (cold) to red (hot). $n_{melt} = 1$ markers (crustal markers) are depicted as black dots.

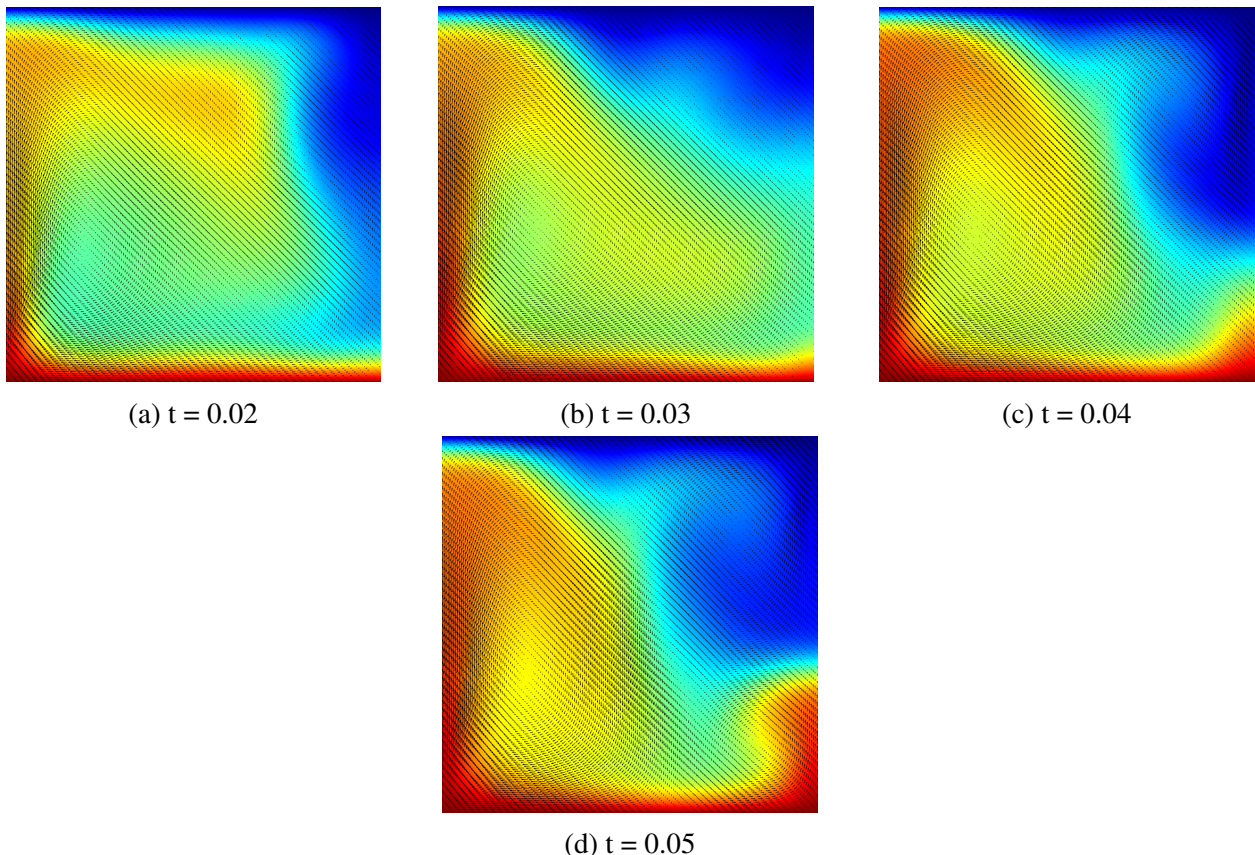


Figure 18: ρ contrast case. Snapshots of model run with the following parameters: $\text{Ra} = 10^5$, $\text{Br} = -0.5$, $\rho = [\text{Br}, 0]$, $\mu = [1, 1]$, melt region = 50/600, $n_{el} = 100$. The velocity field is depicted with small black arrows in the direction of the velocity vector at that point. The temperature is depicted as a colored gradient from blue (cold) to red (hot).

4.0.2 Effect of Aspect Ratio

For this suite of runs, there were bugs that introduced error into the quantity of melt that is generated—based on the placement of new markers in the reseeding process (described in Section 3.3.9), it was easier for markers to cross into the melting depth. Therefore, the absolute position of where melt is generated, and the absolute quantity, may be inaccurate. However, it should still be feasible to analyze these metrics relative to each other, given they were all run under the same conditions.

None of the runs in this suite had markers that evolved when they crossed D_{melt} ; that is, ρ_{inc} , f_{H_2Oinc} , and H_{inc} were all 0. The only variation was the aspect ratio of the box. There were 3 runs:

- Asp 1 (Figure 19): aspect ratio = 1
- Asp 2 (Figure 20): aspect ratio = 2
- Asp 3 (Figure 21): aspect ratio = 3

These runs are similar to the no contrast run in the suite detailed in Section 4.0.1. The main difference between the no contrast run and the Asp 1 run is the implementation of Equation 29 so that viscosity is temperature and depth dependent. D_{melt} was also shallowed significantly, so I will not compare melt production.

As visible for all runs in this suite, the center of the convection cell has been shifted shallower compared to the no contrast run. This is because of the viscosity drop in the upper mantle, allowing rock in the upper mantle to migrate faster than rock in the lower mantle. This also results in rising plume heads being thinner than descending plume heads. This is true for all runs in this suite, where the center of the convection cell is directly below upper-lower mantle boundary.

The minimum viscosity reached by the end of the model runs were similar across the suite ($\text{Log}(\mu') = -0.8$), but the maximum viscosity values varied:

- Asp 1 (Figure 19): $\text{Log}(\mu') = 2.4$
- Asp 2 (Figure 20): $\text{Log}(\mu') = 3.1$
- Asp 3 (Figure 21): $\text{Log}(\mu') = 3.0$

Asp 1 is distinctly lower than Asp 2 and Asp 3. The most viscous area is the lower mantle directly below the upper mantle where there is cold downwelling; it is possible that with a lower aspect ratio, the area of cold downwelling has a restricted viscosity range. With a forcibly smaller convective cell, the hot upwelling warms the cold downwelling, which decreases the viscosity of the downwelling. This is visible in Asp 3 as well, which has two convective cells, one larger and one smaller. The cold downwelling for the larger convective cell results in higher viscosity values in the lower mantle than the smaller.

Asp 1 and Asp 2 both establish a single convection cell; Asp 3 establishes 2. It is possible that varying environments will allow Asp 2 or Asp 1 to establish multiple convection cells, but as of this suite it is necessary to use an aspect ratio of at least 3 in order to explore if having multiple whole mantle convection cells changes rate of crustal formation or mixing patterns.

Although none of the simulations formed any crustal material that was given enough time to participate in downwelling, all of the runs produced visibly different amounts of crustal material, with Asp 1 producing the least and Asp 3 producing the most. All crustal material was generated at sites of upwelling. It then follows that Asp 3 produces the most crust, given that the area for crustal generation is roughly doubled due to the plume head being allowed to expand in both directions, rather than being inhibited by the side of the box. Still, Asp 2 produces more crust than Asp 1 despite both runs only exhibiting one convection cell. When analyzing the rate of crustal building as proposed in Section 3.4.1, it would be useful to weight it by the aspect ratio given that boxes with a larger aspect ratio have more area for crustal generation.

There does not appear to be any critical bias in Asp 1 that would make future runs with an aspect ratio of 1 unviable, but it seems worthwhile to run some runs with an aspect ratio of 3 to continue checking for bias, particularly in terms of quantity of melt production.

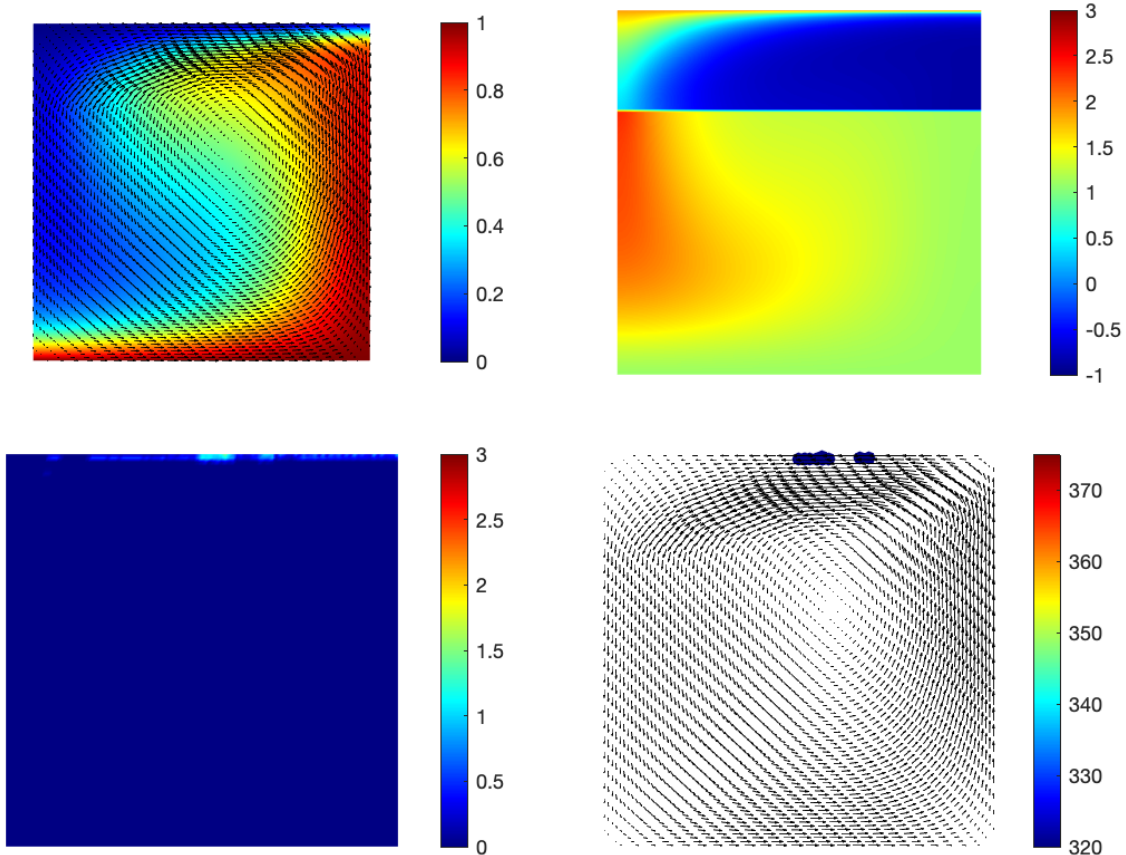


Figure 19: Top left plot: Temperature. Colored gradient from blue (cold) to red (hot). Velocity represented as arrows. Top right plot: Log(viscosity): Colored gradient from blue (low viscosity) to red (high viscosity). Bottom left plot: n_{melt} in the nodes. Colored gradient from blue ($n_{melt} = 0$) to red ($n_{melt} = 3$). Bottom right plot: Velocity represented as arrows and $n_{melt} > 0$ represented as visible dots.

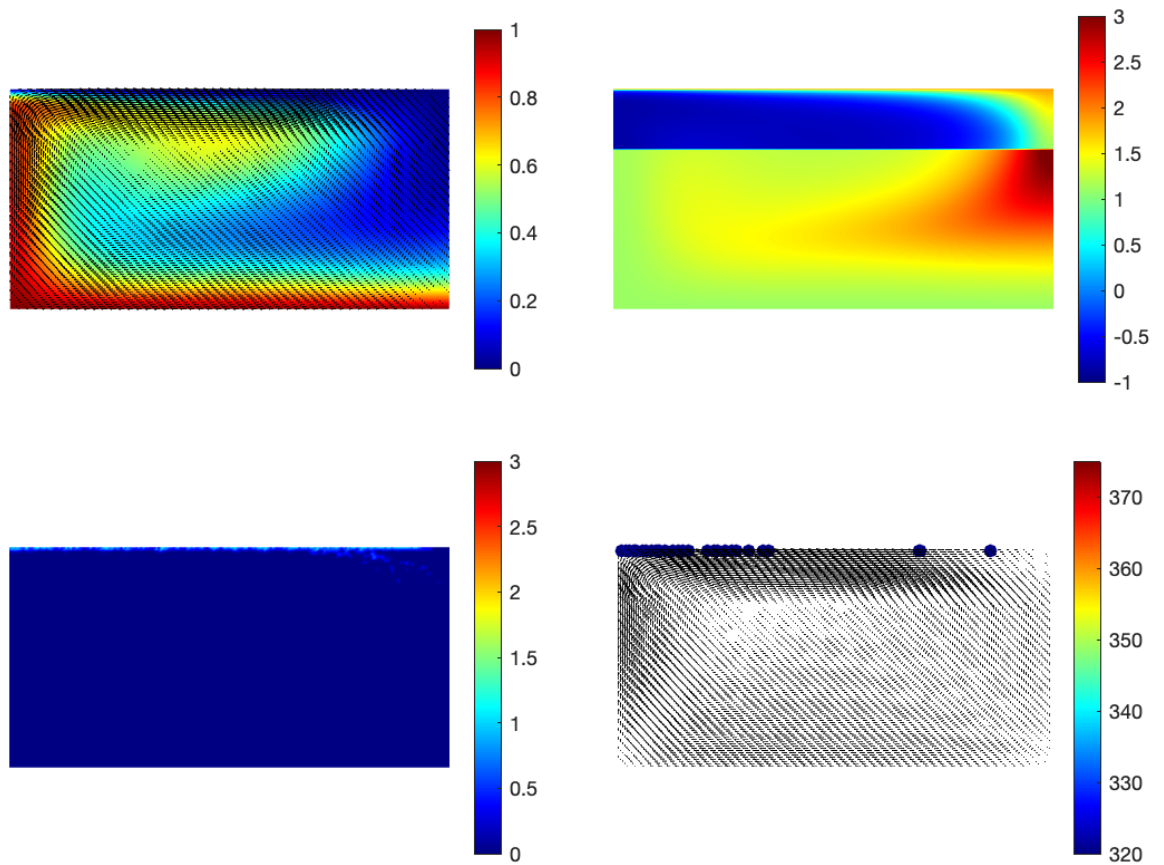


Figure 20: Top left plot: Temperature. Colored gradient from blue (cold) to red (hot). Velocity represented as arrows. Top right plot: Log(viscosity): Colored gradient from blue (low viscosity) to red (high viscosity). Bottom left plot: n_{melt} in the nodes. Colored gradient from blue ($n_{melt} = 0$) to red ($n_{melt} = 3$). Bottom right plot: Velocity represented as arrows and $n_{melt} > 0$ represented as visible dots.

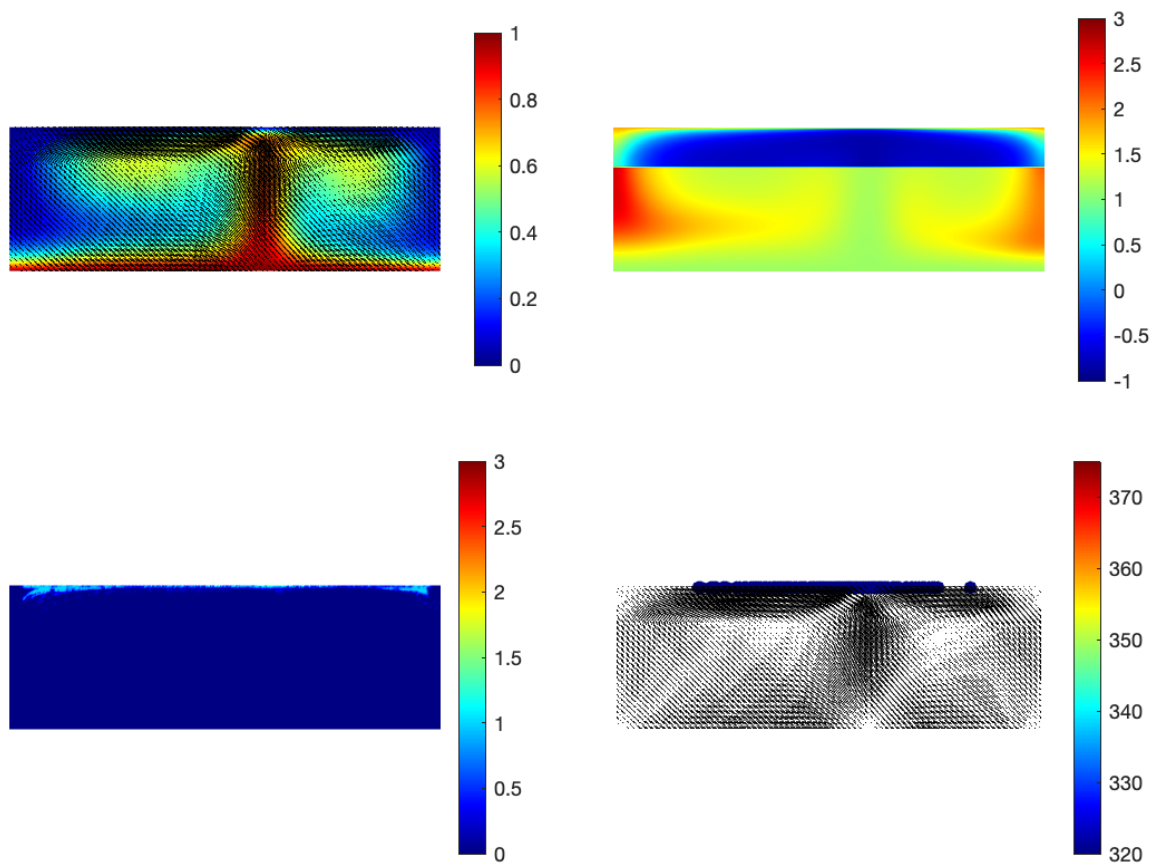


Figure 21: Top left plot: Temperature. Colored gradient from blue (cold) to red (hot). Velocity represented as arrows. Top right plot: Log(viscosity): Colored gradient from blue (low viscosity) to red (high viscosity). Bottom left plot: n_{melt} in the nodes. Colored gradient from blue ($n_{melt} = 0$) to red ($n_{melt} = 3$). Bottom right plot: Velocity represented as arrows and $n_{melt} > 0$ represented as visible dots.

4.0.3 Effect of Water Fugacity

The runs in this suite were run with $D_{melt} = 0$, so there is no evolution of melt to be analyzed. Run parameters are documented in Table 2.

The runs discussed in this section are as follows:

- Fug 0.5 (Figure 22): $f_{H_2Omax} = 0.5$
- Fug 1 (Figure 23): $f_{H_2Omax} = 1$

Note that the mantle rock starts saturated (at f_{H_2Omax}).

Both Fug 1 and Fug 0.5 exhibited only upper mantle convection during the start of the simulation, as pictured in the first subfigure of Figure 22. It can be seen that there are multiple sites of cold, viscous downwelling that are confined to the upper mantle while there is no convection yet established in the lower mantle. Because the upper mantle is less viscous, it is able to initiate convection sooner than the lower mantle. When convection initiates in the lower mantle, the runs exhibit different behavior in the upper mantle.

In Fug 1, the initiation of convection in the lower mantle erases the convective cells that were confined to the upper mantle and establishes whole mantle convection. Both for upwelling and downwelling, there are visible deflections at the upper-lower mantle boundary that were not visible in any of the runs in the Effect of Aspect Ratio suite, described in Section 4.0.2. These deflections impede temperature advection across the upper-lower mantle boundary, resulting in weaker plumes reaching the surface/core-mantle boundary.

Adding in the effect of water fugacity unilaterally dropped the viscosity by over an order of magnitude, which is likely encouraging these deflections. These deflections only occur at the edge of the box; it may be worthwhile to run this simulation at a higher aspect ratio to see if they are a product of the model geometry, or if unilaterally lowered viscosity always yields this pattern.

In Fug 0.5, a stable convective cell remains present over the site of lower mantle upwelling. This cell diverts lower mantle upwelling, similar to the deflection seen in Fug 1, but does not impede heat flow as strongly, pictured best in the temperature plot of the second subfigure in Figure 22. This results in a hotter upper mantle in Fug 0.5 than Fug 1. In the temperature plot of the third subfigure of Figure 22, there are higher temperatures across the upper mantle than there are in the temperature plot of Figure 23, which has run for the same length of simulation time.

The diversion of heat is also noticeable when looking at the surface. There is thinning of the cold surface where the upwelling has been diverted to rather than above the lower mantle upwelling in Figure 22. This is persistent, even when the lower mantle upwelling mixes with the downwelling of the upper mantle convection cell, resulting in a colder upwelling as pictured in the third subfigure.

Fug 0.5, notably different from Fug 1, also exhibits migrating downwellings of the surface that do not penetrate the lower mantle, as seen in the third subfigure of Figure 22. Unlike the convection cell above the lower mantle upwelling, these downwellings produce convection cells that are not stable. The downwelling pictured in the third subfigure continues migrating rightward until it merges with the whole mantle downwelling.

The reason that this downwelling is exhibited in Fug 0.5 but not Fug 1 may be because the temperature of the upper mantle is higher in Fug 0.5 than in Fug 1, which locally increases the Ra (refer to Equation 2) because ΔT is larger for Fug 0.5. However, it is of note that μ may be lower in Fug 1 due to the increased fugacity, though it is not visibly apparent on the plots.

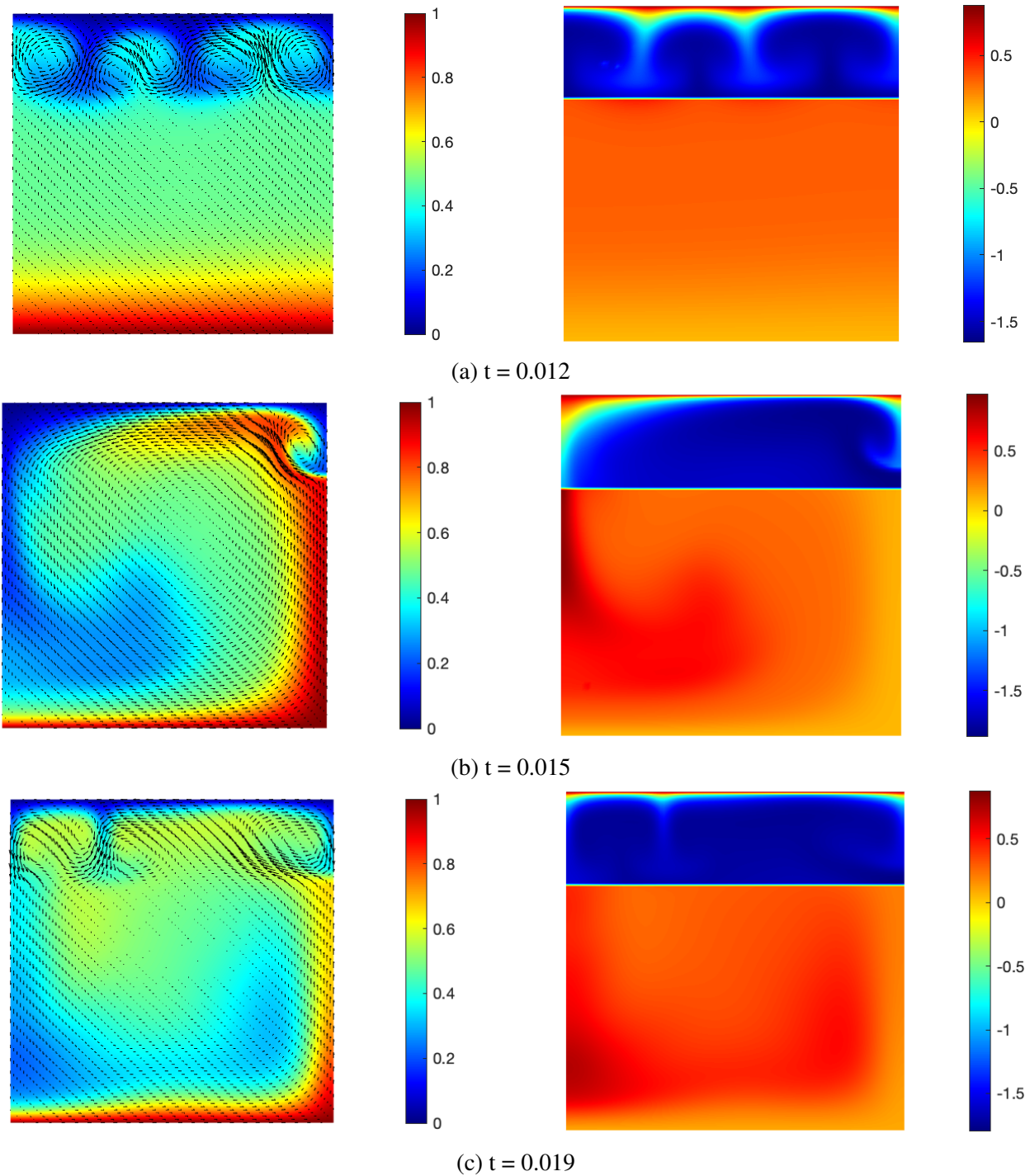


Figure 22: Left plots: Temperature. Colored gradient from blue (cold) to red (hot). Velocity is represented as arrows. Right plot: Viscosity. Colored gradient from blue (low viscosity) to red (high viscosity). Subfigures taken at different times for the same model run. Time given in subfigure caption.

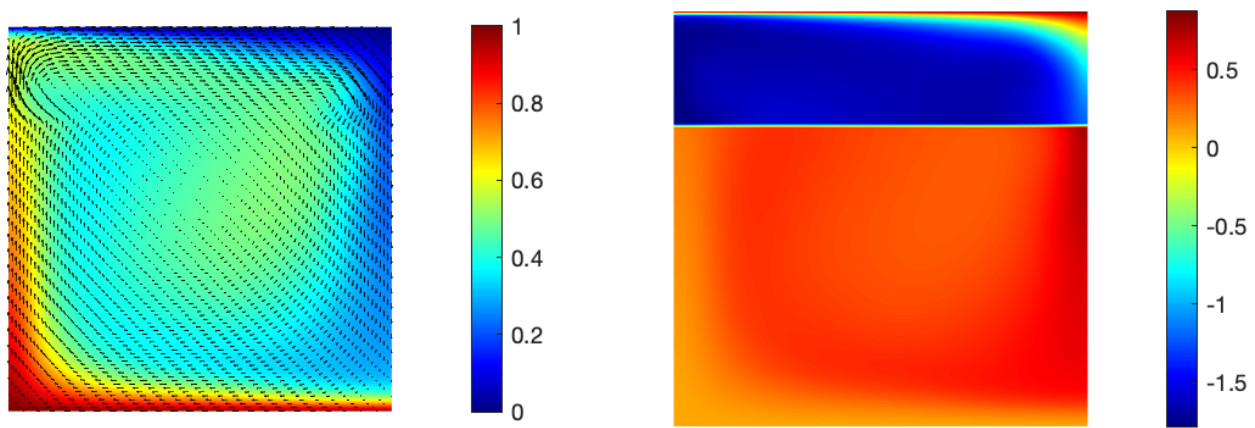


Figure 23: Left plot: Temperature. Colored gradient from blue (cold) to red (hot). Velocity is represented as arrows. Right plot: Viscosity: Colored gradient from blue (low viscosity) to red (high viscosity). $t = 0.020$

4.0.4 Result Table

The following table is a reference for all runs discussed throughout Section 4 and contains all values the simulations were run with.

Suite Name	Run Name	Ra	ρ_{max}	ρ_{inc}	f_{H_2Omax}	f_{H_2Oinc}	H_{min}	H_{max}	H_{inc}	D_{melt}	Resolution	Aspect Ratio	Duration
Effect of Aspect Ratio	Asp 1	$1 \cdot 10^5$	-2	0	1	0	330	370	0	0	50	1	0.02
Effect of Aspect Ratio	Asp 2	$1 \cdot 10^5$	-2	0	1	0	330	370	0	0	50	2	0.02
Effect of Aspect Ratio	Asp 3	$1 \cdot 10^5$	-2	0	1	0	330	370	0	0	50	3	0.02

Table 2: Parameters for model runs. Note: Does not include runs described in Section 4.0.1 due to differing model setup.

References

- Boehnke, P., Bell, E. A., Stephan, T., Trappitsch, R., Keller, C. B., Pardo, O. S., Davis, A. M., Harrison, T. M., Pellin, M. J. (2018). Potassic, high-silica Hadean crust. *Proceedings of the National Academy of Sciences*, 115(25), 6353–6356. <https://doi.org/10.1073/pnas.1720880115>
- Christensen, N. I., Mooney, W. D. (1995). Seismic velocity structure and composition of the continental crust: A global view. *Journal of Geophysical Research: Solid Earth*, 100(B6), 9761–9788. <https://doi.org/10.1029/95JB00259>
- Dong, J., Fischer, R. A., Stixrude, L. P., Lithgow-Bertelloni, C. R. (2021). Constraining the Volume of Earth’s Early Oceans With a Temperature-Dependent Mantle Water Storage Capacity Model. *AGU Advances*, 2(1), e2020AV000323. <https://doi.org/10.1029/2020AV000323>
- Hastie, A. R., Law, S., Bromiley, G. D., Fitton, J. G., Harley, S. L., Muir, D. D. (2023). Deep formation of Earth’s earliest continental crust consistent with subduction. *Nature Geoscience*, 16(9), Article 9. <https://doi.org/10.1038/s41561-023-01249-5>
- Hawkesworth, C. J., Kemp, A. I. S. (2006). Evolution of the continental crust. *Nature*, 443(7113), Article 7113. <https://doi.org/10.1038/nature05191>
- Korenaga, J. (2011). Thermal evolution with a hydrating mantle and the initiation of plate tectonics in the early Earth. *Journal of Geophysical Research: Solid Earth*, 116(B12). <https://doi.org/10.1029/2011JB008410>
- Korenaga, J. (2021). Hadean geodynamics and the nature of early continental crust. *Precambrian Research*, 359, 106178. <https://doi.org/10.1016/j.precamres.2021.106178>
- Lammer, H., Bredehöft, J. H., Coustenis, A., Khodachenko, M. L., Kaltenegger, L., Grasset, O., Prieur, D., Raulin, F., Ehrenfreund, P., Yamauchi, M., Wahlund, J.-E., Grießmeier, J.-M., Stangl, G., Cockell, C. S., Kulikov, Y. N., Grenfell, J. L., Rauer, H. (2009). What makes a planet habitable? *The Astronomy and Astrophysics Review*, 17(2), 181–249. <https://doi.org/10.1007/s00159-009-0019-z>
- Lowe, D. R., Tice, M. M. (2007). Tectonic controls on atmospheric, climatic, and biological evolution 3.5–2.4Ga. *Precambrian Research*, 158(3), 177–197. <https://doi.org/10.1016/j.precamres.2007.04.008>
- Mei, S., Kohlstedt, D. L. (2000). Influence of water on plastic deformation of olivine aggregates: 1. Diffusion creep regime. *Journal of Geophysical Research: Solid Earth*, 105(B9), 21457–21469. <https://doi.org/10.1029/2000JB900179>
- Mulyukova, E. (2015). Stability of the large low shear velocity provinces: Numerical modeling of thermochemical mantle convection [Universität Potsdam]. <https://publishup.uni-potsdam.de/frontdoor/index/index/docId/8222>
- Mulyukova, E., Steinberger, B., Dabrowski, M., Sobolev, S. V. (2015). Survival of LLSVPs for billions of years in a vigorously convecting mantle: Replenishment and destruction of chemical anomaly. *Journal of Geophysical Research: Solid Earth*, 120(5), 3824–3847. <https://doi.org/10.1002/2014JB011688>
- Steinberger, B., Becker, T. (2012). Subduction to the lower mantle—A comparison between geodynamic and tomographic models. *Solid Earth*, 3, 415–432. <https://doi.org/10.5194/se-3-415-2012>
- Tenzer, R., Chen, W., Jin, S. (2015). Effect of Upper Mantle Density Structure on Moho Geometry. *Pure and Applied Geophysics*, 172(6), 1563–1583. <https://doi.org/10.1007/s00024-014-0960-2>
- Thompson, A. B. (1992). Water in the Earth’s upper mantle. *Nature*, 358(6384), Article 6384. <https://doi.org/10.1038/358295a0>
- Todesco, M., Spera, F. J. (1992). Stability of a chemically layered upper mantle. *Physics of the Earth and Planetary Interiors*, 71(1), 85–99. [https://doi.org/10.1016/0031-9201\(92\)90031-P](https://doi.org/10.1016/0031-9201(92)90031-P)